

Far-infrared photometric observations of the outer planets and satellites with Herschel^{*}-PACS

T. G. Müller¹, Z. Balog², M. Nielbock², R. Moreno³, U. Klaas², A. Moór⁴, H. Linz², H. Feuchtgruber¹

¹ Max-Planck-Institut für extraterrestrische Physik, Postfach 1312, Giessenbachstraße, 85741 Garching, Germany

² Max-Planck-Institut für Astronomie, Königstuhl 17, 69117 Heidelberg, Germany

³ Observatoire de Paris, Laboratoire d'Etudes Spatiales et d'Instrumentation en Astrophysique (LESIA), 5 Place Jules Janssen, 92195 Meudon Cedex, France

⁴ Konkoly Observatory, Research Center for Astronomy and Earth Sciences, Hungarian Academy of Sciences; Konkoly Thege 15-17, H-1121 Budapest, Hungary

Received ; accepted

ABSTRACT

We present all Herschel PACS photometer observations of Mars, Saturn, Uranus, Neptune, Callisto, Ganymede, and Titan. All measurements were carefully inspected for quality problems, were reduced in a (semi-)standard way, and were calibrated. The derived flux densities are tied to the standard PACS photometer response calibration, which is based on repeated measurements of five fiducial stars. The overall absolute flux uncertainty is dominated by the estimated 5% model uncertainty of the stellar models in the PACS wavelength range between 60 and 210 μm . A comparison with the corresponding planet and satellite models shows excellent agreement for Uranus, Neptune, and Titan, well within the specified 5%. Callisto is brighter than our model predictions by about 4-8%, Ganymede by about 14-21%. We discuss possible reasons for the model offsets. The measurements of these very bright point-like sources, together with observations of stars and asteroids, show the high reliability of the PACS photometer observations and the linear behavior of the PACS bolometer source fluxes over more than four orders of magnitude (from mJy levels up to more than 1000 Jy). Our results show the great potential of using the observed solar system targets for cross-calibration purposes with other ground-based, airborne, and space-based instruments and projects. At the same time, the PACS results will lead to improved model solutions for future calibration applications.

Key words. Instrumentation: photometers – Methods: data analysis – Space vehicles: instruments – Techniques: photometric – Radiation mechanisms: Thermal – Infrared: planetary systems

1. Introduction

The planets of the solar system and their satellites beyond Earth have surface and brightness temperatures of a few hundred Kelvin and are thereby bright infrared emitters. With radiometers on space probes, such as the infrared radiometer for Mariner (Chase 1969), IRIS on Voyager (Hanel et al. 1980), and the Photopolarimeter-Radiometer (PPR) on Galileo (Russell et al. 1992), accurate information on temperatures, thermal properties, albedo, energy balance, and infrared emission spectra have been collected, making the outer planets and their satellites suitable bright calibration standards. Radio occultation data acquired with Voyager have been used to probe the vertical structure of the planetary atmospheres (Lindal 1992). The inner planets are not accessible to cryogenic space telescopes, since they are inside the solar constraint for these facilities.

In particular, Uranus and Neptune have been established as excellent flux standards for contemporary far-infrared space observatories, providing well-adapted flux levels to the dynamic range of their instrument detectors. Mars, Jupiter, and Saturn are too bright for sensitive photometers, but are observable with far-infrared instruments with high spectral resolution. The SPIRE (Griffin et al. 2010) and PACS (Poglitsch et al. 2010) instruments

onboard the Herschel Space Observatory (Pilbratt et al. 2010) both used Uranus and Neptune, either as prime calibrators in the case of SPIRE (Swinyard et al. 2010), or as complementary calibrators to stellar (Dehaes et al. 2011) and asteroid (Müller et al. 2014) prime calibrators in the case of PACS. For the latter flux calibration scheme, this approach covered a wide flux range to address the non-linear response of the detectors and allowed consistency checks in the case of overlapping fluxes of different calibrator types and reference models. In addition, bright point sources allow obtaining measurements with very high signal-to-noise ratio (S/N) with which different instrument-specific aspects can be characterized, such as point-spread functions, crosstalk, and ghosts. They also serve to determine optimal observing strategies. For the PACS spectrometer, the bright solar system targets helped to establish the in-flight relative spectral response and wavelength calibration.

In preparation of and during the Herschel mission, a number of workshops took place selecting and reviewing the best-suited planet, satellite, asteroid, and stellar flux models, which were applied in support of the absolute photometric calibration.

Here, we provide precise far-infrared photometry of the outer planets Uranus and Neptune and for the planet satellites Callisto, Ganymede, and Titan based on an independent calibration with stellar standards. We perform a thorough comparison with best-suited models, from which feedback and constraints for future improvements is provided.

* *Herschel* is an ESA space observatory with science instruments provided by European-led Principal Investigator consortia and with important participation from NASA.

Our photometry is also a substantial input for cross-calibration aspects, in particular to connect Herschel-PACS calibration with calibration schemes on ground-based (sub-millimeter and millimeter facilities such as ALMA, APEX, or IRAM/NOEMA), with airborne facilities (SOFIA), or other space telescope facilities (ISO, Akari, Spitzer, and Planck).

In Sect. 2 we present the available PACS photometer chop-nod and scan-map observations from the Herschel calibration and science programs. Section 3 explains the data reduction, calibration, and flux extraction procedures. In Sect. 4 we present the observational results and show comparisons with model predictions, in Sect. 5 we discuss the results, and in Sect. 6 we summarize our findings and give a brief outlook. The observation details, instrument configurations, quality aspects, and the Herschel-centric observing geometries are provided in the appendix for completeness.

2. Observations

All measurements resulting in a derived flux presented here are taken from the coordinated PACS calibration plan that was executed over the full mission. Motivation for and classification of individual measurements with respect to the overall calibration strategy are described in the PACS Calibration document¹, the respective PACS Performance Verification Phase Plan², and the PACS Routine (Science) Phase Calibration Plan³, all available from the Herschel Explanatory Library Listings (HELL⁴).

The PACS photometer exploited two filled silicon bolometer arrays with 32×64 pixels (blue camera) and 16×32 pixels (red camera) to perform imaging photometry in the 60 - 210 μm wavelength range. Observations were taken simultaneously in two bands, 60 - 85 μm (blue band with $\lambda_{ref} = 70.0 \mu\text{m}$) or 85 - 130 μm (green band with $\lambda_{ref} = 100.0 \mu\text{m}$) and 130 - 210 μm (red band with $\lambda_{ref} = 160.0 \mu\text{m}$), over a field of view of 1.75' × 3.5', with full beam sampling in each band. Technical details are given in Poglitsch et al. (2010), the description of the chop-nod and scan-map observing techniques are presented in Nielbock et al. (2013) and Balog et al. (2014), respectively, in the PACS Observer's Manual⁵ (Altieri et al. 2011), and references therein.

2.1. PACS chop-nod observations

The originally recommended PACS photometer observing mode for point and compact sources was the chop-nod point-source photometry mode. This mode used the PACS chopper to move the source by about 50'', corresponding to the size of about 1 blue/green bolometer matrix (16 pixels) or the size of about half a red matrix (8 pixels), with a chopper frequency of 1.25 Hz. The nodding is performed by a satellite movement of the same amplitude, but perpendicular to the chopping direction. On each nod-position the chopper executed 3×25 chopper cycles. The three sets of chopper patterns are either on the same array positions (no dithering) or on three different array positions (dither option). Our bright-source observations here were all made with the dither option, where the chopper pattern was displaced in $\pm Y$ -direction (along the chopper direction) by 8.5'' (2 2/3 blue pixels or 1 1/3 red pixels). Each chopper plateau lasted for 0.4 s

(16 readouts on-board), producing four frames per plateau in the down-link. The full 3×25 chopper cycles per nod-position were completed in less than one minute. The pattern was repeated on the second nod-position. When repetition factors exceeded 1 (usually only for fainter targets), the nod-cycles were repeated in the following way (example for four repetitions): nodA-nodB-nodB-nodA-nodA-nodB-nodB-nodA to minimise satellite slew times. Our chop-nod observations were taken either in low or high gain. More details about PACS photometer observations taken in chop-nod mode can be found in Nielbock et al. (2013). Our PACS chop-nod observations are listed in Table A.1 in the appendix.

2.2. PACS scan-map observations

Although originally not designed for point-source observations, the scan-map technique replaced the point-source chop-nod mode. After the science demonstration phase (SDP) it was recommended to use a so-called mini scan-map mode for observations of point and compact sources. The mini scan-map mode had a higher sensitivity and allowed a better characterization of the close vicinity of the target and larger scale structures in the background. Most of the bright-source measurements were executed in the mini scan-map implementation as recommended in the official release note⁶. The satellite scans were usually made with the nominal 20''/s speed (see exceptions in Sect. 2.3 and in Table A.2 in the appendix) in array coordinates of 70° and 110° (along the diagonal of the bolometer arrays). Only a few early measurements were made under different angles of 63° and 117° or 45° and 135°. The scan-map observations have different scan-leg lengths of 2.0' to 7.0', but usually a total of 10 legs and a separation of 4'' between the scan legs. The repetition factor for the mini scan-maps was 1, with the exception of two sets of Neptune measurements where the scan-maps were repeated four times. Some of the scan-map observations were taken in low gain to avoid saturation. Mars was taken in high gain (despite its very high flux) with the goal to characterize the point-spread function (PSF) wings. Here the measurements suffer from saturation in the PSF core and a standard flux determination through aperture photometry is not possible. Another two sets of measurements are related to Saturn and Uranus (see Table A.3), but the planets were located at the edge or even outside the observed field. These measurements are listed, but a flux determination for the planets was not possible. A full description of the scan-map mode and its performance can be found in Balog et al. (2014). The observational details of our PACS scan-map observations are listed in Tables A.2 and A.3.

2.3. Observation quality information

Most of the PACS photometer science and calibration measurements are of very high quality. Only a few measurements suffered from suboptimal instrument settings, instrument or satellite events, or space environment influences. All problematic and quality-related issues are collected in various reports and documents, available from the HELL.

Our sample has two sets of measurements with pointing-critical solar aspect angles (SAA) of the spacecraft: (1) a set of four scan-map observations of Neptune in OD 759 took place at almost -20° SAA; (2) the complete set of four Titan measurements was executed on OD 1138 at -18.3° SAA. A degradation

¹ PCD; PACS-MA-GS-001, Issue 1.10, Nov. 2014.

² PICC-MA-PL-001, Issue 2.0, May 2014.

³ PICC-MA-PL-002, Issue 4.01, May 2014.

⁴ <http://www.cosmos.esa.int/web/herschel>.

⁵ http://herschel.esac.esa.int/Docs/PACS/html/-pacs_om.html

⁶ http://herschel.esac.esa.int/twiki/pub/Public/-PacsCalibrationWeb/PhotMiniScan_ReleaseNote_20101112.pdf

of the pointing performance has been measured for these warm attitudes (Sánchez-Portal et al. 2014), but a correction is not possible at this stage. The astrometry of these Neptune and Titan measurements is therefore less reliable, but there was no influence on the aperture photometry, which was performed directly at the location of the bright source in the final maps.

The PACS photometer calibration is mainly based on observations taken in the nominal satellite scan speed of 20"/s. However, some of the planet observations were executed either with 10"/s or 60"/s scan speed (see Table A.2). Point-source fluxes in different sky fields and based on different satellite scan speeds were analyzed, but no obvious problems were found (see the report on the PACS map-making tools: analysis and benchmarking⁷). The detector response calibration is not affected by the satellite scan speed, but the reliability of the aperture photometry might be slightly reduced for high scan speeds of 60"/s by small differences of a few percent in the encircled energy fraction (EEF) within a given aperture (see also PACC-ME-TN-033⁸, Vers. 2.1 or later). In these cases it is recommended to use relatively large apertures to include the slightly wider PSF. This was done here for our bright sources. We note that specific EEF tables for 60"/s scan speed are in preparation.

Most of our observations have standard instrument settings for chop-nod or scan-map modes; these measurements can easily be found in the HSA, and the pipeline provides reliable products. Only the two observations of Callisto and Ganymede were taken in non-standard settings and the HSA postcards are missing, but the reliability of the corresponding photometry is not affected (see discussion in Sect. 5).

Four Neptune measurements from OD 1097 on May 15, 2012 (OBSIDs 1342245787, 1342245788, 1342245789, and 1342245790) suffered from a failure of the blue SPU⁹; they are labeled "FAILED" in the HSA. The measurements in the red, long-wavelength channel are very likely not affected by this event, but were not available at the time of processing and therefore were not included in our analysis.

After OD 1375 (February 17, 2013) half of the red PACS photometer array was lost (indicated as "red matrix saturated"), but point-source photometry was still possible. Four Neptune measurements from OD 1444 (April 26, 2013; OBSIDs 1342270939, 1342270940, 1342270941, and 1342270942) were affected, but the data are clean otherwise, and aperture photometry was possible in both channels for all four maps.

3. Data reduction, calibration, and photometry

3.1. Processing of chop-nod and scan-map observations

The data reduction and calibration of chop-nod and scan-map data is described in Nielbock et al. (2013) and Balog et al. (2014), respectively. Specific aspects in the analysis of moving solar system targets are addressed in Kiss et al. (2014). To reduce our bright targets, we adjusted a few settings and used very recent software developments for PACS photometer observations. The new corrections and reduction steps are meanwhile part of the standard product generation (SPG) pipelines version 13.0 and higher:

⁷ http://herschel.esac.esa.int/twiki/pub/Public/-PacsCalibrationWeb/pacs_mapmaking_report_ex_sum_v3.pdf

⁸ http://herschel.esac.esa.int/twiki/pub/Public/-PacsCalibrationWeb/bolopsf_21.pdf

⁹ Signal Processing Unit, part of the PACS warm electronics.

- Gyro correction: the latest satellite pointing products include corrections for high-frequency small pointing jitter on the basis of the satellite-internal gyros.
- New calibration file for the focal plane geometry: correcting for very small distortion effects that have not been handled before.
- Flux correction function for chop-nod observations (as given in Nielbock et al. 2013).

Only for scan-map observations:

- Precise timing of the sequential readout of the individual detector columns: the photometer detectors are read out sequentially column by column during a 40 ms cycle. Combined with a satellite scan pattern of 10, 20, or 60"/s, this correction improves the sharpness of the PSF by assigning more accurate pointing information to each individual pixel.
- Larger size of the mask (60" instead of 25" given in Balog et al. 2014) to account for the much more extended PSFs for the bright sources: This mask is used in the context of the high-pass filtering of the data to avoid flux losses for point sources.
- High-pass filtering with a filter width of 15, 20, and 35 readouts in blue, green, and red band, respectively.
- Frame selection based on scan speed (must be within $\pm 10\%$ of the nominal speed).
- Final projection of all data with `photProject()`, using the default pixel fraction (`pixfrac = 1.0`) and reduced map pixel sizes of 1.1", 1.4", and 2.1" in the blue, green, and red channel, respectively.

For each target, each band, and each scan- and cross-scan as well as for each chop-nod data set, we produced calibrated standard data products (maps) in the object-centric reference system.

3.2. Flux extraction and uncertainty estimation

We performed standard aperture photometry (source flux and $1-\sigma$ uncertainty) on each of the final maps. Standard aperture radii of 12", 12", and 22" were used, requiring aperture correction factors of 0.802, 0.776, and 0.817 at 70, 100, and 160 μm , respectively.

3.2.1. Chop-nod measurements

The chop-nod observing technique eliminates the background automatically. The photometric uncertainty was estimated from the fluctuations in a given sky annulus (see details in Nielbock et al. 2013). Correlated noise is corrected by an empirical function to obtain a conservative upper limit for the measurement uncertainties. The relatively large uncertainties can be attributed to the chopping amplitude and the field of view in chop-nod mode observations; both are too small and do not allow determining clean background fields around our very bright sources. Typical flux uncertainties (without the given 5% absolute flux uncertainty from the detector response calibration through prime standard stars) are well below 1% in blue and green, and well below 2% in red.

3.2.2. Scan-map observations

The sources are extremely bright, and a combination of scan- and cross-scan measurements is not needed. We therefore present the extracted fluxes for each observation (OBSID) separately. To estimate the photometric uncertainty in scan-map measurements, we placed apertures with radii of $10''$ in a 7 by 7 grid on the map around the source and measured the underlying fluxes. Then we used σ -clipping to remove the apertures that were contaminated by the source flux (about half of the apertures were eliminated). The final $1\text{-}\sigma$ uncertainty is then the r.m.s. of fluxes from the remaining blank apertures. Typical flux uncertainties (without the given 5% absolute flux uncertainty from the detector response calibration through selected stars) are well below 1% in all three bands.

3.3. Non-linearity correction

Bolometers are thermal detectors where a thermistor converts radiation (or heat) into an electrical signal. The impedance of the thermistor strongly depends on its temperature, and the relation between incoming flux and output voltage is non-linear. During the ground tests of the PACS instrument, this non-linear behavior of the bolometers was extensively characterized for a wide range of incoming fluxes. The non-linearity effects of each individual pixel were fit by simple functions over the relevant range of fluxes (telescope and sky combined) around the in-flight operating point of the bolometers (Billot 2011). These functions are used in the general processing steps of the PACS bolometer to linearize the fluxes: the measured flux in a given pixel and in a given band is multiplied with the corresponding non-linearity correction factor. The correction step is automatically applied by the photometer pipeline in the level 1 data product generation, together with saturation, flat-field, offset, and response calibration.

The non-linearity correction factors are close to 1.0 for almost all photometer observations. This correction is relevant only for the brightest regions in the sky and very bright point sources. For bright point sources - like the calibration asteroids - this correction is between 0 and approximately 6%, depending on the source, band, and pixel (see Müller et al. 2014). For the planets Uranus and Neptune, the correction increases to about 5-15%, while for Callisto and Ganymede the non-linearity factor is 1.17 in the blue band and about 1.05 in the red band.

3.4. Color corrections

For the calculation of the monochromatic flux densities at the PACS photometer reference wavelengths of $70.0\mu\text{m}$, $100.0\mu\text{m}$, and $160.0\mu\text{m}$, it is still required to perform a color correction to account for the difference of a constant energy spectrum $\nu \cdot F_\nu = \lambda \cdot F_\lambda = \text{const.}$ (assumption in the PACS photometer calibration) and the true spectral energy distribution (SED) of the object (Müller et al. 2011a, Balog et al. 2014). Our calculated color-correction factors are listed in Table 1. These correction factors and their estimated uncertainties are based on the listed model spectra.

In the following tables we present the measured and calibrated fluxes together with the monochromatic flux densities after color-correction at the PACS reference wavelengths. The flux uncertainties presented in the tables are measurement errors and do not include the uncertainties in color correction (estimated to be $\approx 1\%$ in most cases, and $\approx 2\%$ for Titan showing many strong lines in the PACS range) nor the absolute flux calibration errors

of 5% (see Balog et al. 2014). These have to be added quadratically when using the derived fluxes in an absolute sense.

4. Observational results and comparison with model predictions

The planet and satellite models were calculated from disk-averaged brightness temperature spectra based on planetary atmosphere models together with the Herschel-centric apparent solid angle at the time of the observations. Various model versions were prepared in support for the Herschel mission by model experts and provided to the Herschel Calibration Steering Group. Specific model versions have then been used by the three instrument teams for observation planning and specific calibration purposes. Figure 1 shows the model predictions for Uranus, Neptune, Callisto, Ganymede, and Titan either at the epoch of the Herschel-PACS measurement or - for Uranus and Neptune - as minimum-maximum prediction for all observing epochs.

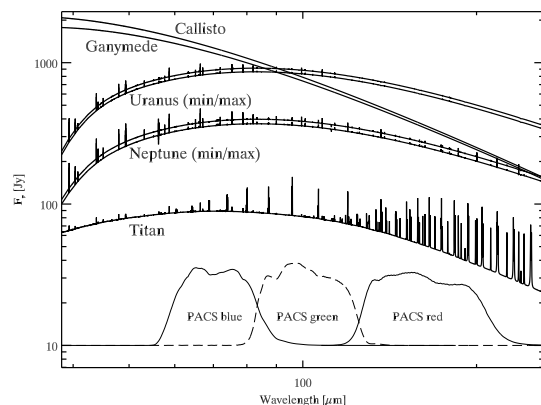


Fig. 1. Absolute disk-integrated model flux density predictions for Callisto, Ganymede, and Titan in the Herschel-centric reference system and at the epoch of the corresponding PACS measurements. The minimum-maximum model predictions for Uranus ("ura_esa2_2_i.dat") and Neptune refer to all available PACS measurements during the entire Herschel mission. The PACS band-passes are shown in arbitrary units. The blue, green, and red bands have peak transmissions of 51%, 56%, and 46%, respectively.

4.1. Mars

The main goal of the Mars observations with the PACS photometer was to characterize the PSF wings and to probe for ghosts and stray-light features in the field of view (see D. Lutz 2012, PICC-ME-TN-033¹⁰, Vers. 2.1). The data were therefore taken in high-gain. The scan legs are much longer and the leg separation much wider than in standard mini scan-map observations in order to map out the PSF characteristics at large distances. The central source parts (several arcsec wide) are flagged as completely saturated in all final maps¹¹. For completeness reasons

¹⁰ http://herschel.esac.esa.int/twiki/pub/Public/-PacsCalibrationWeb/bolopsf_21.pdf

¹¹ Using a pre-Herschel delivery of a Mars model "mars_esa_2_i.dat", combined with the true Herschel-centric diameter of Mars gives model flux predictions of $\approx 44\,000$ to $54\,000\text{ Jy}$ at $70\mu\text{m}$, $\approx 25\,000$ to $30\,000\text{ Jy}$

Table 1. Color-correction factors (cc) for our bright sources. Models are taken from <ftp://ftp.sciops.esa.int/planets/originalData/>. The estimated maximal uncertainty for these corrections is 2% for Titan and about 1% for the rest of the targets.

Source	cc _{70.0μm}	cc _{100.0μm}	cc _{160.0μm}	unc. [%]	model source
Mars	0.947	1.033	1.054	≈ 1	mars_esa_2_i.dat (Moreno)
Uranus	0.984	0.995	1.018	≈ 1	orton_uranus_esa5 (Orton)
Uranus	0.984	0.992	1.019	≈ 1	ura_esa2_2_i.dat (Moreno)
Neptune	0.984	0.993	1.020	≈ 1	nep_esa5_2_i.dat (Moreno)
Callisto	0.998	1.016	1.055	≈ 1	call_esa2_2_i.dat (Moreno)
Ganymede	0.996	1.014	1.053	≈ 1	gany_esa2_2_i.dat (Moreno)
Titan	0.985	1.002	1.028	≈ 2	tit_esa3_2_i.dat (Moreno)
fiducial stars	1.016	1.033	1.074	≈ 1	Balog et al. (2014)

we present the detailed observation information in Table A.2 in the appendix.

4.2. Uranus

Table 2 contains the reduced and calibrated fluxes of all Uranus observations obtained with the Herschel-PACS photometer. Each line is connected to an output map that is related to a single OBSID based either on a single scan direction or a single chop-nod observation. The observing geometry and relevant instrument and satellite configuration parameters are given in Tables A.1 and A.2. The absolute calibrated flux densities (column "Flux") are based on a flat energy spectrum ($\nu F_\nu = \text{const.}$) with uncertainties coming from the signal processing and aperture photometry of the final maps. The color-corrected flux densities at the PACS reference wavelength are given in column FD_{cc} , where color-correction factors from Table 1 were used. The model predictions are based on two different models that are both relevant for different purposes in the context of PACS and SPIRE photometer and spectrometer calibration: (i) the Uranus model "orton_uranus_esa5_model_spectrum.txt", which was taken from the HCalSG web pages and was provided by Glenn Orton, JPL/NASA (Orton et al. 2014); (ii) the Uranus model "ura_esa2_2_i.dat", which was taken from the HCalSG web pages at <ftp://ftp.sciops.esa.int/planets/originalData/esa2/> and was provided by R. Moreno in 2009 (see also Moreno et al. 2016, in preparation). Both models of Uranus were used to check the PACS calibration. They are connected to slightly different thermal structures: for Uranus "esa2" (available at the beginning of the Herschel mission) the thermal profiles go back to Voyager radio-occultation measurements (Pearl et al. 1990; Lindal et al. 1992), while for Uranus "esa5" measurement constraints from mid- and far-IR (Spitzer-IRS and Herschel/SPIRE; Orton et al. 2014) were also considered. The radiative transfer modeling includes continuum opacities from collision-induced absorption of H₂, He, and CH₄. "esa5" is more tuned toward the SPIRE wavelengths and was not tested so far against PACS data. The brightness temperature differences between the two models are below 5% in the PACS wavelength range. The model uncertainties are linked mainly to the input parameters and therefore reflect the absolute calibration accuracy. The model brightness temperatures were combined with Uranus' angular diameter as seen from Herschel, taking the equatorial and polar radii and the sub-observer latitude (i.e., Ob-

lat in JPL/Horizon) into account¹². The last column of Table 2 contains the calculated ratio between FD_{cc} and the corresponding model prediction at the given reference wavelength. The final observation-to-model ratios are shown in Figs. 2 (model by Moreno) and 3 (model by Orton). The two PACS observing modes - chop-nod and scan-map techniques - are shown with different symbols and at slightly shifted wavelengths ($\pm 2\mu\text{m}$) for better visibility. The absolute uncertainties for both Uranus models were estimated to be 5%, similar to the stellar model uncertainties for the five fiducial stars. The $\pm 5\%$ boundaries are shown as dashed lines in Figs. 2, 3, 4, and 7.

4.3. Neptune

Table 3 contains the reduced and calibrated fluxes of all Neptune observations obtained with the Herschel-PACS photometer. Each line is connected to an output map that is related to a single OBSID based either on a single scan direction or a single chop-nod observation. The observing geometry and the relevant instrument and satellite configuration parameters are given in Tables A.1 and A.2. The absolute calibrated flux densities (column "Flux") are based on a flat energy spectrum ($\nu F_\nu = \text{const.}$) with uncertainties coming from the signal processing and aperture photometry of the final maps. The color-corrected flux densities at the PACS reference wavelength are given in column FD_{cc} , where color-correction factors from Table 1 were used. The model predictions are based on the Neptune model "nep_esa5_2_i.dat" (production in 2014), which was taken from the HCalSG web pages at <ftp://ftp.sciops.esa.int/planets/originalData/esa5/>. The radiative transfer modeling includes continuum opacities from collision-induced absorption of H₂, He, and CH₄. The thermal profiles go back to Voyager measurements (Pearl & Conrath 1991, Lindal et al. 1992) and fit the IR measurements of Akari spectra of Neptune's stratosphere (Fletcher et al. 2010). The Neptune model also fits the line-to-continuum ratio (i.e., relative measurements) of SPIRE and PACS spectra including CO and HD lines (Moreno et al. 2016, in preparation). The model brightness temperatures were combined with Neptune's angular diameter as seen from Herschel, taking into account the equatorial and polar radii and the sub-observer latitude (see footnote in Sect. 4.2). The last column of Table 3 contains the calculated ratio between FD_{cc} and the corresponding model prediction at the given reference wave-

at 100 μm , and $\approx 11\,000$ to 14 000 Jy at 160 μm for the Herschel observing epochs.

¹² It is worth noting that the angular diameter values from the JPL-Horizons system correspond to the equatorial diameters, which are about 0.7% (Neptune) and 1.0% (Uranus) larger than our calculated geometric diameters, and the JPL values would produce too high model fluxes ($\approx 2\%$ too high for Uranus and $\approx 1.4\%$ too high for Neptune).

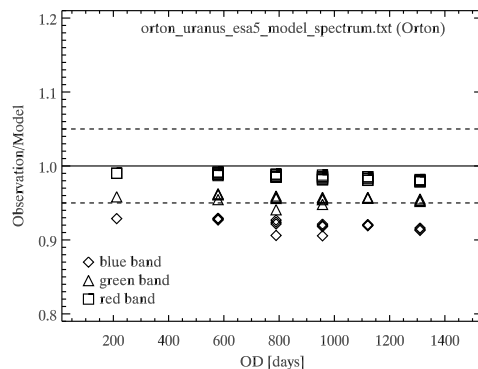
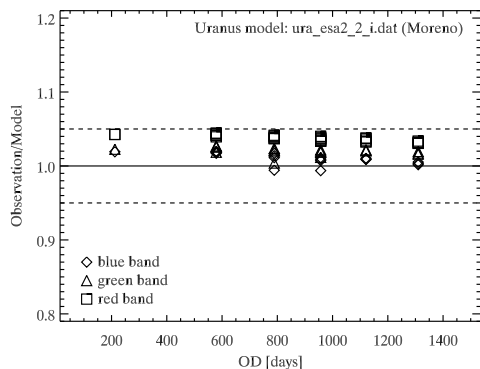
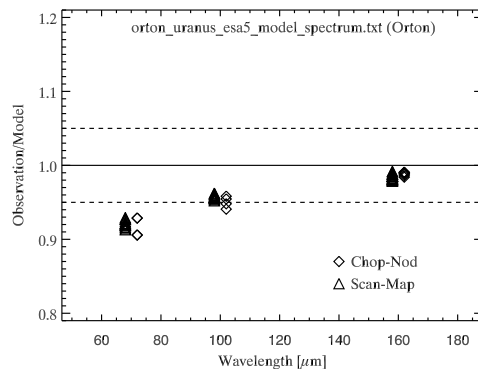
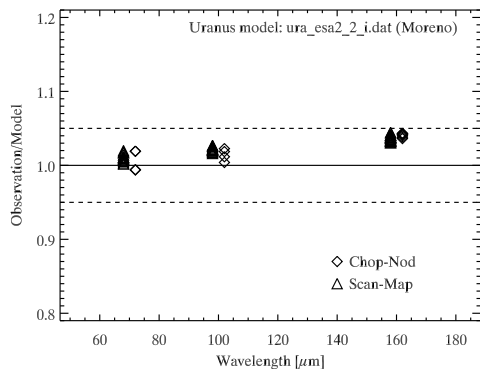


Fig. 2. All PACS photometer observations of Uranus divided by the corresponding model predictions by R. Moreno. Top: as a function of wavelength (chop-nod and scan-map observations are shown with different symbols). Bottom: as a function of OD.

Fig. 3. All PACS photometer observations of Uranus divided by the corresponding model predictions by G. Orton. Top: as a function of wavelength (chop-nod and scan-map observations are shown with different symbols). Bottom: as a function of OD.

length. The final observation-to-model ratios are shown in Fig. 4. The two PACS observing modes - chop-nod and scan-map techniques - are shown with different symbols and at slightly shifted wavelengths ($\pm 2 \mu\text{m}$) for better visibility. The absolute uncertainties for the Neptune model were estimated to be 5%, similar to the stellar model uncertainties for the five fiducial stars.

4.4. Callisto, Ganymede, and Titan

The two point-like Jupiter moons Callisto and Ganymede are so bright (each $> 1000 \text{ Jy}$ at $70 \mu\text{m}$) that they allow instantaneous determination of their brightness peaks within the time resolution of a bolometer frame (10 Hz). The scan-map observations from OD 981 were used to determine the relative positions of the bolometer matrix pixels, the size of the matrix gaps, rotation angles of the matrices, and distortion effects. The measurements were performed when the two moons were at the farthest possible distance from Jupiter (Callisto at $351\text{--}361''$ and Ganymede at $303\text{--}304''$ from Jupiter's body center, with Jupiter having an apparent Herschel-centric size of $40.7''$).

Titan, the largest moon of Saturn, was observed as part of the PACS photometer flux calibration program in the context of linearity checks and cross-calibration in the intermediate flux regime. It was observed when it was at the largest separation

from Saturn at $183''$, with Saturn having an apparent Herschel-centric size of $17.7''$ (see Fig. 6).

Table 7 summarises the apparent motions, sizes, and angular separations during the PACS observations. The Callisto and Ganymede observations were executed in orthogonal scan directions of 0° and 90° with respect to the array orientation to cope with possible timing problems. The measurements were also taken in support of pointing jitter assessment during scans and have 4 Hz star tracker telemetry available. The Titan measurements were taken in standard scan- and cross-scan observations.

The model of Titan (`tit_esa3_2_i.dat`¹³ by Moreno) was computed using the radiative transfer model for a disk-averaged geometry, described in Courtin et al. (2011) and Moreno et al. (2012). This model includes continuum opacities from collision-induced absorption of $\text{N}_2\text{--CH}_4$ pairs and uses the thermal profile from Huygens probe measurements (Fulchignoni et al. 2005) combined with CIRS measurements (Vinatier et al. 2010). Molecular lines of CO, HCN, and CH_4 and their isotopes are

¹³ available from <ftp://ftp.sciops.esa.int/planets/-originalData/esa3/> and soon from the Herschel Explanatory Library Listings (HELL) at <http://www.cosmos.esa.int/web/-herschel>

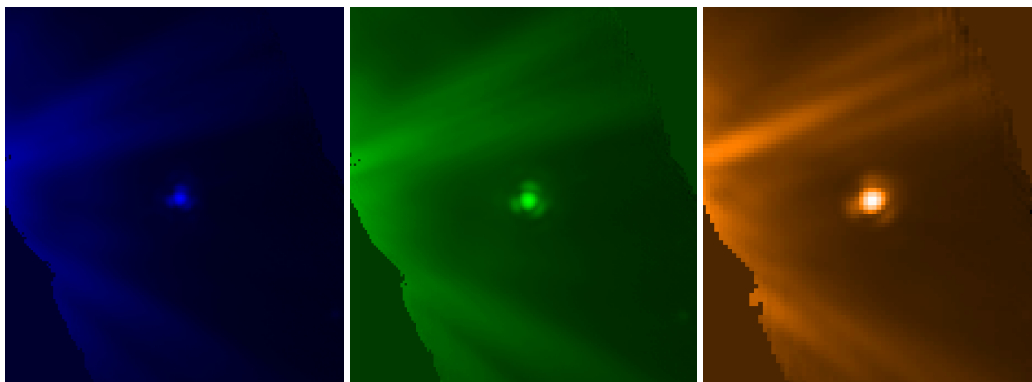


Fig. 6. Titan measurement with the PACS photometer at 70, 100, and 160 μm . Titan was located about 3 arcmin from Saturn. Saturn's PSF wings are visible, but did not influence the photometry significantly.

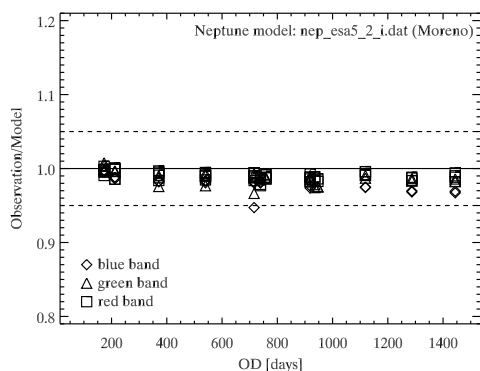
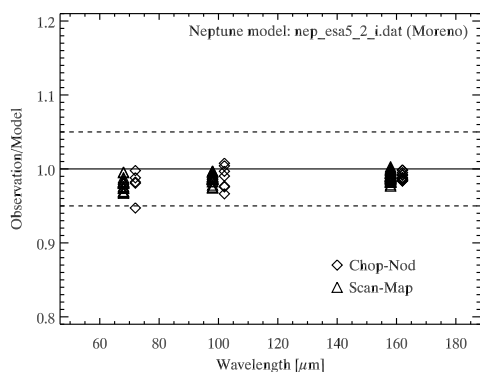


Fig. 4. All PACS photometer observations of Neptune divided by the corresponding model predictions by R. Moreno. Top: as a function of wavelength (chop-nod and scan-map observations are shown with different symbols). Bottom: as a function of OD.

included, as are the HIFI and SPIRE observations. The final absolute accuracy is better than 5% for Titan.

The disk-averaged models of Callisto (`call_esa2_2_i.dat`¹⁴ by Moreno) and Ganymede



Fig. 5. Combined Callisto and Ganymede measurement with the PACS photometer at 70 μm . The two sources were separated by about 55'' and moved with different apparent motions (see Table 7) at the time of the observations. Top: PACS observing frames centered on Callisto (right source). Bottom: centered on Ganymede (left source). The angular separation is about 6' between Jupiter and Callisto and about 5' between Jupiter and Ganymede, with an apparent angular diameter of Jupiter of 40.7''.

(`gany_esa2_2_i.dat`¹⁵ by Moreno) are based on thermal models of the sub-surface computed upon the Spencer et al. (1989) algorithm. The models solve the heat diffusion equation in the planetary surface material as a function of longitude, latitude, and depth. The thermal inertia used was originally derived by Spencer (1987) from two-layer models and based on 10-20 μm data from Voyager. These models also include the surface dielectric constant and roughness, which are fit from the ground-based measurements at mm-wavelength performed with the IRAM-PdBI and the SMA (Moreno et al. 2008). The model accuracies were estimated to be better than 7% for Ganymede and Callisto. Effectively, Callisto and Ganymede continuum

¹⁴ available from <ftp://ftp.sciops.esa.int/planets/-originalData/esa2/>

¹⁵ available from <ftp://ftp.sciops.esa.int/planets/-originalData/esa2/>

models are not very accurate in the PACS wavelength range. This is probably linked to the effective albedo and different thermal inertia layers in the sub-surface, which are very difficult to constrain from disk-averaged observations.

The model brightness temperatures were combined with the angular diameters (as seen by Herschel and as listed by JPL/Horizon system under "Ang-diam") of these three satellites and calculated for the precise observing epoch. The penultimate columns of Tables 4, 5, and 6 contain the calculated ratio between FD_{cc} and the corresponding model prediction at the given reference wavelength. The final observation-to-model ratios are shown in Fig. 7.

5. Discussions

Table 8 summarizes all observation-to-model ratios, their scatter, and the number of available observations. Most of the ratios are very close to 1.0, which shows an excellent agreement between the flux densities derived from the PACS photometer measurements and the corresponding model predictions. The standard deviations of these ratios are very small - in many cases well below 1% - for a given object and within a given band. This confirms the very high stability of the PACS bolometer response over the entire mission lifetime (see also Balog et al. 2014, Müller et al. 2014, or Nielbock et al. 2013). The small standard deviations are even more impressive knowing that the reference measurements on the PACS internal calibration sources were not even used in the reduction and calibration process (see Moór et al. 2014). Neptune observations were taken in low- and high-gain mode (see Tables A.1 and A.2), but no differences in the corresponding observation-to-model ratios can be found. It is also worth noting that the ratios derived from the chop-nod mode and the scan-map mode agree within 1%, showing that the reduction and correction procedures are very well balanced for these very different observing techniques, and for both gain settings.

5.1. Callisto, Ganymede, and Titan

The Callisto and Ganymede fluxes seem to be systematically higher by 5-20% than the corresponding model predictions. In contrast, Titan agrees very well with the expected fluxes. We investigated different aspects to determine whether there are technical reasons or model shortcomings that might explain the disagreement for Callisto and Ganymede.

The Callisto and Ganymede measurements were taken in non-tracking mode, and to produce the maps shown in Fig. 5, it was necessary to stack all frames first on the expected position of Callisto (top right in Fig. 5) and then on Ganymede (bottom left in Fig. 5). Overall, the final maps look very clean and flat, and possible stray-light or Jupiter PSF interferences¹⁶ are entirely eliminated by the high-pass filtering reduction and the background subtraction in the aperture photometry step. In addition, for Titan - with an angular separation of only about 3' from Saturn during the PACS measurements - there are no significant stray-light or PSF contributions in the aperture photometry (see Fig. 6). The derived fluxes of the Saturn and Jupiter satellites are not influenced by the proximity of the planets.

Callisto and Ganymede were separated by 55'' at the time of the measurements (see Table 7). We calculated the mutual contribution of the far-field PSF flux distribution within our photometry apertures of 12'' and 22'' in radius. But the flux contri-

¹⁶ Callisto was about 6' away from Jupiter, Ganymede only about 5'.

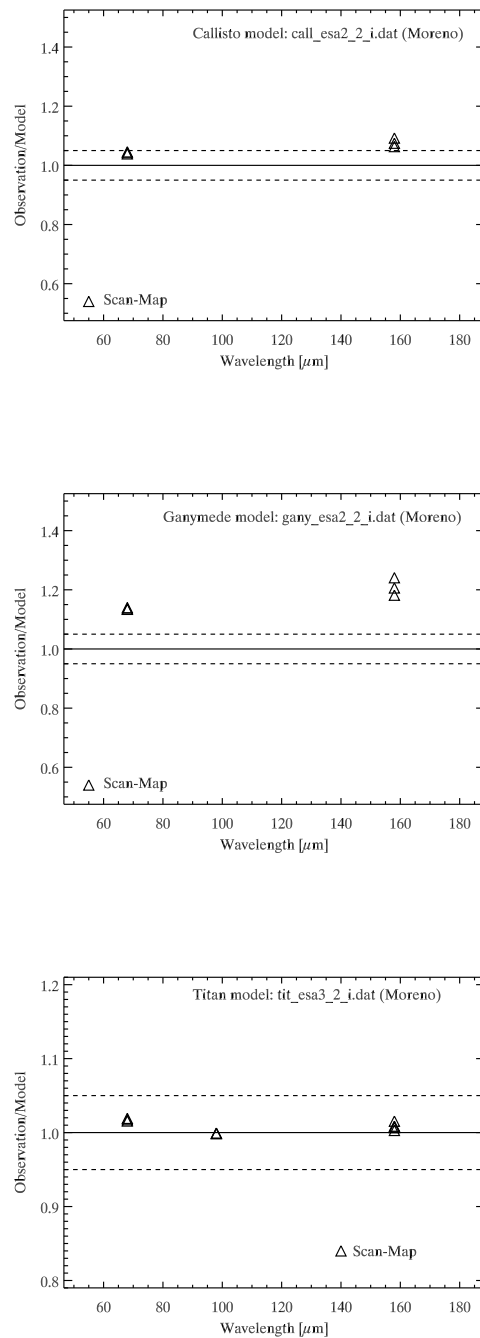


Fig. 7. All PACS photometer observations of Callisto, Ganymede, and Titan, divided by the corresponding model predictions and as a function of wavelength. Top: Callisto. Middle: Ganymede. Bottom: Titan.

bution of Callisto at the location of Ganymede (and vice versa) is well below 1% at 70 μm and also at 160 μm. The obtained aperture fluxes are therefore reliable despite the proximity of bright sources.

The measurements were taken with a satellite scan speed of 10''/s (instead of the nominal 20''/s). But the slow scan speed had no impact on the final fluxes either. We tested the stability of the source fluxes by using a range of different aperture sizes, but the resulting fluxes were all within 1%, confirming the negligible

Table 4. Observational results of the Herschel-PACS photometer observations of Callisto. Columns are described in the text, the brightness temperatures T_b^{obs} were calculated from the observed fluxes, the apparent effective size, and the total absolute flux uncertainties (see Sect. 5).

OD	OBSID(s)	observ. mid-time	PACS Band	Flux [Jy]	Unc. [Jy]	λ_{ref} [μm]	FD_{cc} [Jy]	FD_{model} [Jy]	Ratio $\text{FD}_{cc}/\text{FD}_{model}$	T_b^{obs} [K]
scan-map:										
981	1342238042	2455946.74716	B	1324.792	3.772	70.0	1327.447	1272.926	1.04	147.7 \pm 5.6
981	1342238042	2455946.74716	R	416.483	3.289	160.0	394.771	371.255	1.06	146.0 \pm 6.5
981	1342238043	2455946.77907	B	1328.038	8.141	70.0	1330.699	1272.554	1.05	147.8 \pm 5.6
981	1342238043	2455946.77907	R	427.658	12.807	160.0	405.363	371.146	1.09	148.9 \pm 6.7

Table 5. Observational results of the Herschel-PACS photometer observations of Ganymede.

OD	OBSID(s)	observ. mid-time	PACS Band	Flux [Jy]	Unc. [Jy]	λ_{ref} [μm]	FD_{cc} [Jy]	FD_{model} [Jy]	Ratio $\text{FD}_{cc}/\text{FD}_{model}$	T_b^{obs} [K]
scan-map:										
981	1342238042	2455946.74716	B	1321.756	4.899	70.0	1327.064	1168.363	1.14	134.3 \pm 4.8
981	1342238042	2455946.74716	R	442.907	4.670	160.0	420.614	355.936	1.18	134.0 \pm 5.8
981	1342238043	2455946.77907	B	1326.010	7.710	70.0	1331.335	1167.895	1.14	134.5 \pm 4.8
981	1342238043	2455946.77907	R	464.826	15.927	160.0	441.430	355.793	1.24	138.8 \pm 6.1

Table 6. Observational results of the Herschel-PACS photometer observations of Titan.

OD	OBSID(s)	observ. mid-time	PACS Band	Flux [Jy]	Unc. [Jy]	λ_{ref} [μm]	FD_{cc} [Jy]	FD_{model} [Jy]	Ratio $\text{FD}_{cc}/\text{FD}_{model}$	T_b^{obs} [K]
scan-map:										
1138	1342247418	2456104.14470	B	89.380	0.656	70.0	90.741	89.029	1.02	76.8 \pm 1.6
1138	1342247419	2456104.14470	B	89.066	0.530	70.0	90.422	89.029	1.02	76.7 \pm 1.6
1138	1342247420	2456104.15278	G	81.484	0.583	100.0	81.321	81.451	1.00	79.0 \pm 2.2
1138	1342247421	2456104.15278	G	81.538	0.593	100.0	81.375	81.451	1.00	79.0 \pm 2.2
1138	1342247418	2456104.14874	R	53.901	2.810	160.0	52.433	51.981	1.01	82.8 \pm 3.0
1138	1342247419	2456104.14874	R	53.788	2.955	160.0	52.323	51.981	1.01	82.7 \pm 3.0
1138	1342247420	2456104.14874	R	53.853	2.612	160.0	52.386	51.981	1.01	82.8 \pm 3.0
1138	1342247421	2456104.14874	R	54.259	2.975	160.0	52.781	51.981	1.02	83.1 \pm 3.0

influence of the slower scan speed (see also D. Lutz, PICC-ME-TN-033¹⁷, Vers. 2.1: the baseline for the calculation of aperture encircled energy fractions was a set of bright-source measurements including observations with 10 and 20"/s scan speed).

Callisto and Ganymede are at very high flux levels and the non-linearity correction on signal level is significant. While this correction is in the order of 0-6% for asteroids (Müller et al. 2014) and 5-15% for the planets Uranus and Neptune, it is about 17% for the two Galilean satellites in the blue band and 5-6% in the red band. The true uncertainty of this correction is unknown, but it seems to be very reliable for Uranus and Neptune, for which the non-linearity corrections lead to an excellent agreement between observations and models. The non-linearity corrections for Callisto and Ganymede are only marginally larger, and there is no reason that a slightly larger correction would introduce additional errors. The non-linearity corrections are almost identical for Callisto and Ganymede, and therefore they cannot account for the offset difference seen between the two targets in Fig. 7. A conservative estimate of the quality of the non-linearity correction leads to an additional error of $\approx 5\%$ when the correction is above 15% (applicable for Uranus, Neptune, Callisto, and Ganymede in the blue and green bands) and well below ($\approx 2\%$) for smaller corrections in the red band (see also PICC-

NHSC-TR-031¹⁸). These uncertainties - together with the 5% absolute flux uncertainty and the small uncertainty introduced by colour correction - have to be considered when using the PACS absolute fluxes for model adjustments.

The HSA provides additional well-calibrated measurements of Titan and Callisto taken by the SPIRE spectrometer (Griffin et al. 2010; Swinyard et al. 2010). First, we extracted the Titan spectrometer observations (SPG version 13.0.0) from OD 404 (OBSID 1342198925) and OD 803 (OBSID 1342224755) and compared the observed continuum level with the "tit_esa3_2_i.dat" model prediction using the apparent effective sizes of 0.7460" and 0.7131", respectively. On average, the SPIRE spectrometer continuum fluxes of Titan are about 5% higher than the corresponding model predictions. This agrees well with our observation-to-model ratios for Titan (see Tables 6 and 8) considering the 5% absolute flux accuracy of PACS and SPIRE and the very different calibration schemes for the two instruments. In a second step, we repeated this procedure for Callisto. The reduced and calibrated SPIRE spectrometer data from OD 602 (OBSID 1342212340) were extracted from the HSA. The model calculations based on "call_esa2_2_i.dat" and an apparent effective size of 1.29" led to observation-to-model ratios of 1.10-1.15, very close to the PACS 160 μm ratio of 1.08. This exercise confirms our confidence in the derived PACS fluxes and

¹⁷ http://herschel.esac.esa.int/twiki/pub/Public/PacsCalibrationWeb/bolopsf_21.pdf

¹⁸ available from the Herschel Explanatory Library Listings (HELL) at <http://www.cosmos.esa.int/web/herschel>

Table 7. Summary of the motions, sizes, and separations of Callisto, Ganymede, Titan, Jupiter, and Saturn at start and end times of the PACS observations.

Object	Time	dRA*cosD/dt ¹ ["/h]	d(DEC)/dt ¹ ["/h]	ang-sep ² ["]	Ang-diam ³ ["]
Callisto	2012 Jan 20 05:30	17.21	7.73	361.0	1.37
	2012 Jan 20 07:00	17.36	7.78	351.6	1.37
Ganymede	2012 Jan 20 05:30	11.68	5.87	304.2	1.50
	2012 Jan 20 07:00	12.28	6.10	303.1	1.50
Jupiter	2012 Jan 20 05:30	11.48	5.18	—	40.73
	2012 Jan 20 07:00	11.51	5.19	—	40.72
Titan	2012 Jun 25 15:22	-0.27	0.05	183.1	0.758
	2012 Jun 25 15:45	-0.25	0.05	183.1	0.758
Saturn	2012 Jun 25 15:22	-0.18	-0.57	—	17.74
	2012 Jun 25 15:45	-0.18	-0.57	—	17.74

Notes. ⁽¹⁾ The change rate of the target center apparent RA and DEC (airless). d(RA)/dt is multiplied by the cosine of the declination ; ⁽²⁾ target-primary angular separation. The angle between the center of target object and the center of the primary body it revolves around, as seen by the observer ; ⁽³⁾ the equatorial angular width of the target body full disk, if it were fully visible to the observer .

Table 8. Summary of all observation-to-model ratios, their scatter, and the number of available observations.

Object	Obs. Mode	blue band			green band			red band			Model Version
		average	stdev	num	average	stdev	num	average	stdev	num	
Uranus	CN	1.007	0.015	4	1.014	0.008	4	1.041	0.002	8	ura_esa2_2_i.dat (Moreno)
Uranus	SM	1.011	0.005	15	1.021	0.003	15	1.037	0.004	25	ura_esa2_2_i.dat (Moreno)
Uranus	Both	1.010	0.008	19	1.020	0.005	19	1.038	0.004	33	ura_esa2_2_i.dat (Moreno)
Uranus	CN	0.917	0.013	4	0.950	0.008	4	0.988	0.002	8	orton_uranus_esa5 (Orton)
Uranus	SM	0.921	0.005	15	0.957	0.003	15	0.984	0.004	25	orton_uranus_esa5 (Orton)
Uranus	Both	0.920	0.007	19	0.956	0.005	19	0.985	0.004	33	orton_uranus_esa5 (Orton)
Neptune	CN	0.979	0.019	5	0.988	0.016	7	0.990	0.005	12	nep_esa5_2_i.dat (Moreno)
Neptune	SM	0.980	0.008	20	0.987	0.006	28	0.990	0.006	48	nep_esa5_2_i.dat (Moreno)
Neptune	Both	0.980	0.011	25	0.987	0.009	35	0.990	0.006	60	nep_esa5_2_i.dat (Moreno)
Callisto	SM	1.042	0.003	3	—	—	—	1.077	0.015	3	call_esa2_2_i.dat (Moreno)
Ganymede	SM	1.137	0.003	3	—	—	—	1.210	0.030	3	gany_esa2_2_i.dat (Moreno)
Titan	SM	1.017	0.003	2	0.999	0.001	2	1.010	0.004	4	tit_esa3_2_i.dat (Moreno)

indicates that problems with the models are the main cause of the derived observation-to-model ratios for Callisto and Ganymede.

A closer inspection of the Callisto and Ganymede model-setups immediately revealed a first possible cause for the lower model fluxes. The brightness temperatures in both models refer to a heliocentric distance of 5.21 AU, but the PACS Callisto and Ganymede measurements were taken at 4.98 AU heliocentric distance. As a consequence, the temperature at the sub-solar point is higher by a factor of about 1.02, which influences the model brightness temperatures. This correction would improve the agreement between observed Callisto fluxes and model predictions. We estimated that the new Callisto ratios would then be at 1.05 or below in both PACS bands. For Ganymede the offset would shrink slightly, but the new observation-to-model ratios would still be around 1.1 at 70 μm and slightly above 1.15 at 160 μm . But Ganymede is in general more difficult to model correctly over the entire wavelength range (i.e., from IR to radio). Especially the thermal inertias of the sub-surface layers of Ganymede are not well understood.

To facilitate the usage of our derived and well-calibrated fluxes, we also provide brightness temperatures (see Col. T_b in

Tables 4, 5, and 6) using Planck's law under the assumption of a black body. First, the apparent effective diameter D is translated into a solid angle Ω [sr] = $(D ["/] / 2)^2 \cdot \pi \cdot 2.3504 \cdot 10^{-11}$. This allows calculating the surface brightness B_v [MJy/sr] = F_v^{obs} [Jy] $\cdot 1.0 \cdot 10^{-6} \cdot \Omega^{-1}$. The brightness temperature T_b [K] at a given wavelength λ [μm] is then given by

$$T_b^{-1} = \ln((1 \cdot 10^{25} \cdot 2 \cdot h \cdot c \cdot \lambda^{-3}) / B_v + 1) \cdot \frac{k \cdot \lambda}{h \cdot c}$$

with the speed of light $c = 2.99792458 \cdot 10^{14}$ $\mu\text{m/s}$, the Planck constant $h = 6.6262 \cdot 10^{-27}$ erg-s, and the Boltzmann constant $k = 1.3807 \cdot 10^{-16}$ erg-K⁻¹.

The uncertainties in T_b are calculated from the total flux uncertainties: (i) 5% in absolute flux calibration; (ii) 1% or 2% in colour correction; (iii) and the non-linearity correction: 0%, if the correction is well below 5%, 2%, if the non-linearity correction is around 5%, and 5%, if the correction is well above 10%. The summed flux uncertainties are then between 5% and 7% for Callisto, Ganymede, and Titan in the three PACS bands. Overall, the Titan fluxes agree extremely well with the "tit_esa3_2_i.dat" model by Moreno, no adjustments are necessary. The Callisto

model requires slight modifications to account for the smaller heliocentric distance of the PACS measurement. We expect that this will also lead to a good agreement between observations and model within the given error bars. Only Ganymede shows a mismatch, and the observed fluxes are 10-20% higher than model predictions. Our PACS fluxes are therefore an important legacy and key element for future model updates, for instance, for calibration purposes of ground-based and airborne sub-millimeter and millimeter projects like ALMA, IRAM, or LMT.

5.2. Uranus

The observations of Uranus agree well with the Moreno-based predictions within the given 5-7% model accuracy. But the Uranus model of Orton ("orton_uranus_esa5") shows problems in the short-wavelength PACS range. The model predictions are too high by about 8% at $70\mu\text{m}$ and still about 4-5% too high at $100\mu\text{m}$. The overall impression is that the model seems to work well at the longest PACS wavelength range and also in the SPIRE range (see Bendo et al. 2013, Griffin et al. 2013). The reason for the offset might be related to the He/H₂ ratio used in the model (Orton, priv. comm.). Here, the PACS data will place new and very important constraints on this fundamental property in the Uranus atmosphere.

5.3. Neptune

The observed Neptune fluxes agree within 1-2% with the Moreno "esa5" model predictions. Considering that the PACS photometer fluxes are tied to stellar models and the SPIRE photometer calibration is based on Neptune, our analysis of Neptune shows that PACS and SPIRE produce reliable fluxes on the same absolute level (well within 5%).

5.4. Influence of spectral features

Several planetary objects show spectral features (notably, Neptune and Titan, see Fig. 1), related to minor species (nitriles and water). HCN and H₂O were taken into account for Neptune's model. H₂O has some strong but narrow lines around $60\mu\text{m}$, but with a negligible contribution of less than 0.01% of the PACS continuum. The HCN contribution is about ten times smaller. In the model for Titan, CH₃CN and HC₃N are also narrow and negligible at wavelengths below $300\mu\text{m}$ because of their high rotational J number and lower energy levels $> 1000\text{cm}^{-1}$, which are difficult to populate at atmospheric temperatures of about 150 K.

In summary, these minor species (nitriles and water) do not contribute significantly in the PACS range because (i) the linewidths of these species are very narrow; (ii) the line intensities of CH₃CN and HC₃N decrease strongly with decreasing wavelength below $300\mu\text{m}$. We estimated that within the photometer spectral bandwidth, the contribution is below 0.01% of the total flux and is therefore negligible.

5.5. Non-linearity correction

The results for Uranus, Neptune, and Callisto show the reliability of the PACS fluxes in the high-flux regime where the bolometer response is already in the non-linear regime. The PACS photometer pipeline products and the various reduction scripts take care of non-linearity corrections in a reliable way and point-source fluxes up to 1400 Jy are validated. The rare cases of even brighter sources (where non-linearity corrections of larger than

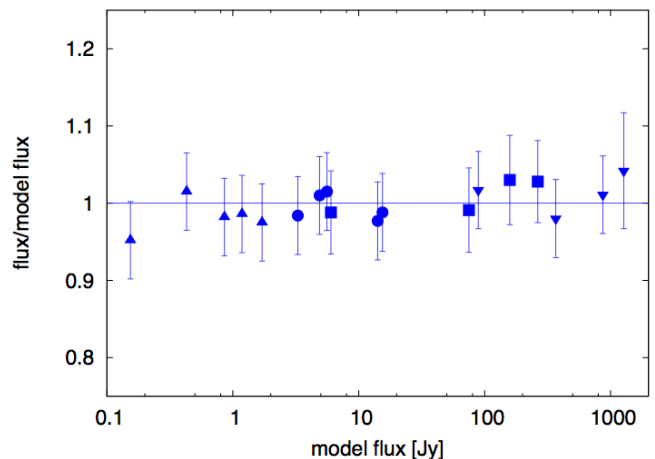


Fig. 8. Reduced and calibrated blue-band fluxes of faint stars (triangles), fiducial stars (circles), prime asteroids (squares), planets (Uranus and Neptune) and satellites Callisto and Titan (reversed triangles), divided by their corresponding model fluxes and shown as a function of model flux.

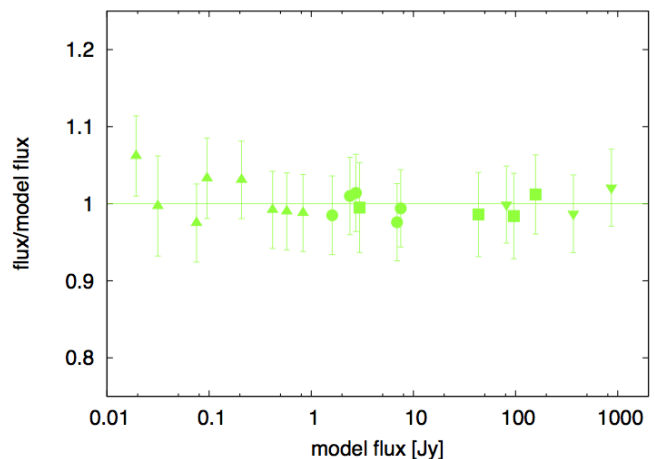


Fig. 9. Reduced and calibrated green-band fluxes of stars, asteroids, planets, satellites, divided by their corresponding model fluxes and shown as a function of model flux.

20% are needed) are formally not verified. However, the pre-flight pixel-by-pixel non-linearity response calibration provides at least a good first-order correction, and the derived flux densities for point-sources above 1400 Jy up to the ADC¹⁹ saturation limit are reliable on an estimated 10% level or better.

In Figs. 8, 9, and 10 we show the observation-to-model ratios for objects spanning 4-5 orders of magnitude in flux. The ratios for the stars are taken from Balog et al. (2014), Nielbock et al. (2013), and Klaas et al. (in preparation). The ratios for the asteroids are taken from Müller et al. (2014), the remaining from our Table 8. In all three PACS bands we find a very good agreement with stellar, asteroid, planet, and satellite models from well below 100 mJy to fluxes well above 1000 Jy. There are also no offsets between low- and high-gain observations, fixed or solar system targets, measurements taken in chop-nod or in scan-map mode, or between PACS and SPIRE photometric measurements.

¹⁹ analog-to-digital converter

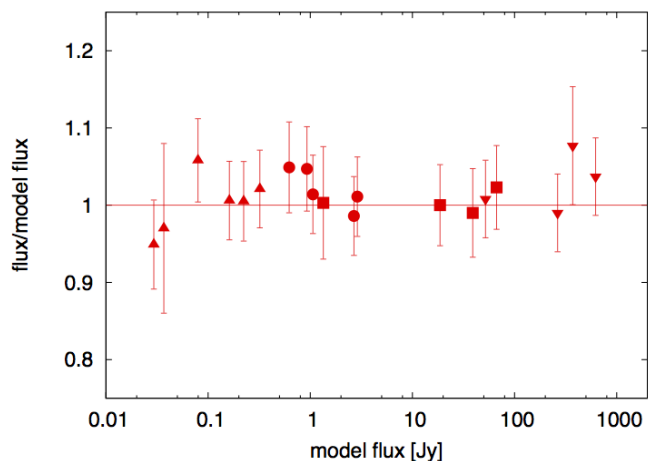


Fig. 10. Reduced and calibrated red-band fluxes of stars, asteroids, planets, satellites, divided by their corresponding model fluxes and shown as a function of model flux.

5.6. Cross calibration

From our experience with asteroids (Müller et al. 2014), and now also from the work on planets and satellites, we conclude that the stellar-based absolute flux calibration of the PACS photometer agrees very well with the Neptune-based photometer calibration of SPIRE (Bendo et al. 2013). The PACS photometer data presented here are crucial for future model updates of Uranus, Callisto, and Ganymede, which are mainly based on radiometry done by interplanetary missions. Improved models are needed for high-frequency amplitude calibration of ALMA and other submm projects. These bright point-sources are also excellent cross-calibration targets for the PACS and SPIRE spectrometers and for SOFIA-FORCAST or FIFI-LS as well.

6. Summary and outlook

We present the PACS photometer observations of bright satellites and planets, mainly taken as part of the coordinated instrument calibration program. These measurements - some of them also taken in non-standard instrument configurations - show the high reliability of the PACS photometer chop-nod and scan-map fluxes: absolute flux densities are given with an absolute flux error of 5% and a relative (repeatability) error of 1-2%. It is important to note here that the absolute calibration of our derived fluxes is tied to five fiducial stars (Balog et al. 2014), and they are therefore completely independent of planet, asteroid, or satellite model predictions.

The comparison with planet and satellite model predictions shows that the established corrections - mainly the non-linearity correction, flux correction for chop-nod data, aperture corrections, or color corrections - are accurate and can be applied as recommended in the PACS handbook and data reduction guides. These corrections are also validated up to the highest flux levels just below the level of ADC saturation. Overall, the PACS photometer standard reduction and calibration procedures lead to reliably calibrated flux densities for point sources ranging from a few milli-Jansky up to about 1000 Jy.

The observations of Neptune and Titan show excellent agreement - within the assigned 5% absolute accuracy - with available models. The Uranus, Callisto, and Ganymede observations indicate that the latest available models have some problems in the PACS wavelength range: The latest Uranus model ("esa5")

shows a wavelength-dependent offset of about 10% at $70\mu\text{m}$, but an acceptable agreement (within 5%) at $160\mu\text{m}$. For Callisto it is the opposite: the model shows a 5% agreement at $70\mu\text{m}$ and is about 10% too low at the long wavelengths. The Ganymede model underestimates the observed and calibrated fluxes by 15 to 25%.

The final tabulated fluxes and the observed brightness temperatures can now be used for future model updates and dedicated studies of surface and atmosphere effects of planets and satellites. Improved model solutions are also relevant in the context of cross calibration between space-based, airborne, and ground-based facilities. These bright point sources are also very important for various calibration activities for ALMA and other astronomical sub-millimeter and millimeter projects.

Acknowledgements. The entire PACS-ICC calibration team is acknowledged for countless contributions in the preparation, conduction, and evaluation process related to the observations of bright point sources. We would also like to thank Nicolas Billot for his feedback on the non-linearity corrections, which are based on PACS pre-launch test campaigns in 2006-2007, and small adjustments for the final in-flight detector bias settings. Glenn Orton, Martin Burgdorf, and Anthony Marston provided help with the planet and satellite models and contributed to the discussions of the results. A. Moór was supported by the Momentum grant of the MTA CSFK Lendület Disk Research Group. PACS has been developed by a consortium of institutes led by MPE (Germany) and including UVIE (Austria); KUL, CSL, IMEC (Belgium); CEA, OAMP (France); MPIA (Germany); IFSI, OAP/AOT, OAA/CAISMI, LENS, SISSA (Italy); IAC (Spain). This development has been supported by the funding agencies BMVIT (Austria), ESA-PRODEX (Belgium), CEA/CNES (France), DLR (Germany), ASI (Italy), and CICYT/MCYT (Spain). SPIRE has been developed by a consortium of institutes led by Cardiff University (UK) and including Univ. Lethbridge (Canada); NAOC (China); CEA, LAM (France); IFSI, Univ. Padua (Italy); IAC (Spain); Stockholm Observatory (Sweden); Imperial College London, RAL, UCL-MSSL, UKATC, Univ. Sussex (UK); and Caltech, JPL, NHSC, Univ. Colorado (USA). This development has been supported by national funding agencies: CSA (Canada); NAOC (China); CEA, CNES, CNRS (France); ASI (Italy); MCINN (Spain); SNSB (Sweden); STFC, UKSA (UK); and NASA (USA). This work was supported by the Hungarian OTKA grant K104607. We thank the anonymous referee for constructive comments.

References

- Altieri, B. (2011), PACS Observer's Manual, HERSCHEL-HSC-DOC-0832, v. 2.4, Dec. 22, 2011, http://herschel.esac.esa.int/Docs/PACS/html/pacs_om.html
- Balog, Z., Müller, T. G., Nielbock, M. et al. 2014, *Exp. Astronomy*, 37, 129
- Bendo, G. J., Griffin, M. J., Bock, J. J. et al. 2013, *MNRAS*, 433, 3062
- Billot, N. 2011, PICC-NHSC-TR-031, Feb. 2011, available from the Herschel Explanatory Library Listings (HELL) at <http://www.cosmos.esa.int/web/herschel>
- Chase, S. C., Jr. 1969, *Applied Optics* 8, 639
- Courtin, R., Swinyard, B. M., Moreno, R. et al. 2011, *A&A*, 536, L2
- Dehaes, S., Bauwens, E., Decin, L. et al. 2011, *A&A* 553, 107
- Fletcher, L. N., Drossart, P., Burgdorf, M. et al. 2010, *A&A*, 514, A17
- Fulchignoni, M., Ferri, F., Angrilli, F. et al. 2005, *Nature*, 438, 785-791
- Griffin, M. J., Abergel, A., Abreu, A. et al. 2010, *A&A*, 518, 3G
- Griffin, M. J., North, C. E., Schulz, B. et al. 2013, *MNRAS*, 434, 992
- Hanel, R., Crosby, D., Herath, L. et al. 1980, *Applied Optics* 19, 1391
- Kiss, C., Müller, T. G., Vilenius, E. et al. 2014, *Exp. Astronomy*, 37, 161
- Lindal, G. F. 1992, *AJ*, 103, 967-982
- Lutz, D. 2012, PACS photometer point spread function, PICC-ME-TN-033, v. 2.1, June 8, 2015, http://herschel.esac.esa.int/twiki/pub/Public/PacsCalibrationWeb/bolopsf_21.pdf
- Moór, A., Müller, T. G., Kiss, C. et al. 2014, *Exp. Astronomy*, 37, 225-238
- Moreno, R., Gurwell, M. A., Moullet, A. et al. 2008, AAS/Division for Planetary Sciences Meeting Abstracts #40, *Bulletin of the American Astronomical Society*, 40, 478
- Moreno, R., Lellouch, E., Lara, L. M. et al. 2012, *Icarus*, 221, 753-767
- Müller, T. G., Okumura, K., Klaas, U. 2011, PACS Photometer Passbands and Colour Correction Factors for Various Source SEDs, PICC-ME-TN-038, v. 1.0, April 12, 2011, http://herschel.esac.esa.int/twiki/pub/Public/PacsCalibrationWeb/cc_report_v1.pdf
- Müller, T. G., Balog, Z., Nielbock, M. et al. 2014, *Exp. Astronomy*, 27, 253
- Nielbock, M., Müller, T. G., Balog, Z. et al. 2013, *Exp. Astronomy*, 36, 631
- Orton, G. S., Fletcher, L. N., Moses, J. I. et al. 2014, *Icarus*, 243, 494-513
- Pearl, J. C., Conrath, B. J., Hanel, R. A., Pirraglia, J. A. 1990, *Icarus* 84, 12
- Pearl, J. C., Conrath, B. J. 1991, *J. Geophys. Research Supp.*, 96, 18921
- Pilbratt, G. L., Riedinger, J. R., Passvogel, T. et al. 2010, *A&A*, 518, L1
- Poglitsch, A., Waelkens, C., Geis, N. et al. 2010, *A&A*, 518, L2
- Russell, E. E., Brown, F. G., Chandos, R. A. et al. 1992, *Space Science Reviews* 60, 531
- Sánchez-Portal, M., Marston, A., Altieri, B. et al. 2014, *Exp. Astronomy*, 37, 453
- Spencer, J. R. 1987, PhD, The University of Arizona, 81S
- Spencer, J. R., Lebofsky, L. A., Sykes, M. V. et al. 1989, *Icarus*, 78, 337-354
- Swinyard, B. M., Ade, P., Baluteau, J.-P. et al. 2010, *A&A*, 518, 4S
- Vinatiev, S., Bézard, B., Nixon, C. A. et al. 2010, *Icarus*, 205, 559-570

Table 2. Observational results of the Herschel-PACS photometer observations of Uranus and comparison with two different models (see Text).

OD	OBSID	observ. mid-time	PACS Band	Flux [Jy]	Unc. [Jy]	λ_{ref} [μm]	FD _{cc} [Jy]	FD _{moreno} [Jy]	Ratio FD _{cc} /FD _{model}	Moreno Orton
chop-nod:										
212	1342188056	2455178.12069	B	864.812	0.486	70.0	878.874	862.299	1.02	0.93
212	1342188056	2455178.12069	R	657.711	9.139	160.0	645.447	619.000	1.04	0.99
212	1342188057	2455178.12340	G	873.153	1.815	100.0	880.195	860.737	1.02	0.96
212	1342188057	2455178.12340	R	657.576	9.022	160.0	645.315	619.000	1.04	0.99
579	1342211116	2455544.21598	B	870.285	1.572	70.0	884.436	867.964	1.02	0.93
579	1342211116	2455544.21598	R	661.492	9.246	160.0	649.158	623.067	1.04	0.99
579	1342211119	2455544.22774	G	875.409	1.798	100.0	882.469	866.343	1.02	0.95
579	1342211119	2455544.22774	R	662.397	8.880	160.0	650.046	623.031	1.04	0.99
789	1342223981	2455754.55343	B	866.861	1.521	70.0	880.956	886.077	0.99	0.91
789	1342223981	2455754.55343	R	672.918	8.103	160.0	660.371	636.069	1.04	0.99
789	1342223984	2455754.56491	G	880.840	1.638	100.0	887.944	884.473	1.00	0.94
789	1342223984	2455754.56491	R	675.109	8.154	160.0	662.521	636.069	1.04	0.99
957	1342235628	2455922.43656	B	837.225	1.405	70.0	850.838	856.257	0.99	0.91
957	1342235628	2455922.43656	R	649.040	8.481	160.0	636.938	614.662	1.04	0.98
957	1342235631	2455922.45609	G	857.702	1.480	100.0	864.619	854.657	1.01	0.95
957	1342235631	2455922.45609	R	651.405	8.372	160.0	639.259	614.627	1.04	0.99
scan-map:										
579	1342211117	2455544.22060	B	871.064	1.869	70.0	885.228	867.964	1.02	0.93
579	1342211118	2455544.22464	B	868.696	1.858	70.0	882.821	867.964	1.02	0.93
579	1342211120	2455544.23128	G	882.701	1.504	100.0	889.820	866.343	1.03	0.96
579	1342211121	2455544.23532	G	881.411	1.770	100.0	888.519	866.343	1.03	0.96
579	1342211117	2455544.22060	R	659.878	1.674	160.0	647.574	623.067	1.04	0.99
579	1342211118	2455544.22464	R	662.876	1.508	160.0	650.516	623.067	1.04	0.99
579	1342211120	2455544.23128	R	660.905	1.646	160.0	648.582	623.031	1.04	0.99
579	1342211121	2455544.23532	R	663.046	1.515	160.0	650.683	623.031	1.04	0.99
789	1342223982	2455754.55794	B	886.706	2.181	70.0	901.124	886.077	1.02	0.93
789	1342223983	2455754.56198	B	881.724	2.457	70.0	896.061	886.077	1.01	0.92
789	1342223985	2455754.56862	G	898.301	2.007	100.0	905.545	884.473	1.02	0.96
789	1342223986	2455754.57266	G	895.208	1.795	100.0	902.427	884.473	1.02	0.96
789	1342223982	2455754.55794	R	672.098	1.731	160.0	659.566	636.069	1.04	0.98
789	1342223983	2455754.56198	R	674.463	1.364	160.0	661.887	636.069	1.04	0.99
789	1342223985	2455754.56862	R	672.173	1.744	160.0	659.640	636.069	1.04	0.98
789	1342223986	2455754.57266	R	674.248	1.578	160.0	661.676	636.069	1.04	0.99
957	1342235629	2455922.44924	B	851.802	2.365	70.0	865.652	856.207	1.01	0.92
957	1342235630	2455922.45328	B	848.719	2.329	70.0	862.519	856.207	1.01	0.92
957	1342235632	2455922.45992	G	866.423	1.220	100.0	873.410	854.657	1.02	0.96
957	1342235633	2455922.46396	G	863.524	1.516	100.0	870.488	854.657	1.02	0.95
957	1342235629	2455922.44924	R	647.260	1.633	160.0	635.191	614.627	1.03	0.98
957	1342235630	2455922.45328	R	650.070	1.472	160.0	637.949	614.627	1.04	0.99
957	1342235632	2455922.45992	R	647.276	1.632	160.0	635.207	614.627	1.03	0.98
957	1342235633	2455922.46396	R	649.832	1.485	160.0	637.715	614.627	1.04	0.99
1121	1342246772	2456086.68500	B	830.384	2.274	70.0	843.886	835.178	1.01	0.92
1121	1342246773	2456086.68904	B	828.958	2.260	70.0	842.437	835.178	1.01	0.92
1121	1342246774	2456086.69308	G	845.147	1.872	100.0	851.963	833.666	1.02	0.96
1121	1342246775	2456086.69712	G	844.028	2.608	100.0	850.835	833.714	1.02	0.96
1121	1342246772	2456086.68500	R	630.782	1.643	160.0	619.021	599.531	1.03	0.98
1121	1342246773	2456086.68904	R	633.665	1.283	160.0	621.850	599.531	1.04	0.98
1121	1342246774	2456086.69308	R	630.943	1.667	160.0	619.179	599.531	1.03	0.98
1121	1342246775	2456086.69712	R	634.054	1.282	160.0	622.232	599.566	1.04	0.99
1310	1342257193	2456275.57361	B	873.132	2.372	70.0	887.329	882.711	1.01	0.92
1310	1342257194	2456275.57765	B	870.025	2.327	70.0	884.172	882.661	1.00	0.91
1310	1342257195	2456275.58169	G	891.126	2.181	100.0	898.312	881.062	1.02	0.96
1310	1342257196	2456275.58573	G	887.978	2.013	100.0	895.139	881.062	1.02	0.95
1310	1342257193	2456275.57361	R	665.387	1.675	160.0	652.980	633.652	1.03	0.98
1310	1342257194	2456275.57765	R	667.418	1.524	160.0	654.974	633.616	1.03	0.98
1310	1342257195	2456275.58169	R	665.408	1.677	160.0	653.001	633.616	1.03	0.98

continued on next page

Table 2. *continued*

OD	OBSID	observ. mid-time	PACS Band	Flux [Jy]	Unc. [Jy]	λ_{ref} [μm]	FD _{cc} [Jy]	FD _{moreno} [Jy]	Ratio FD _{cc} /FD _{model}	Moreno Orton
1310	1342257196	2456275.58573	R	666.522	1.506	160.0	654.094	633.616	1.03	0.98

Table 3. Observational results of the Herschel-PACS photometer observations of Neptune.

OD	OBSID	observ. mid-time	PACS Band	Flux [Jy]	Unc. [Jy]	λ_{ref} [μm]	FD_{cc} [Jy]	FD_{model} [Jy]	Ratio $\text{FD}_{cc}/\text{FD}_{model}$
chop-nod:									
173	1342186637	2455138.56756	B	366.939	0.612	70.0	372.905	373.735	1.00
173	1342186637	2455138.56756	R	272.863	3.096	160.0	267.513	267.860	1.00
173	1342186638	2455138.57417	G	372.860	0.580	100.0	375.488	373.938	1.00
173	1342186638	2455138.57417	R	271.858	3.087	160.0	266.527	267.860	1.00
173	1342186643	2455138.58808	G	374.152	0.573	100.0	376.790	373.938	1.01
173	1342186643	2455138.58808	R	272.697	3.160	160.0	267.350	267.860	1.00
212	1342188052	2455178.10290	G	354.153	0.734	100.0	356.650	357.790	1.00
212	1342188052	2455178.10290	R	257.683	3.417	160.0	252.630	256.293	0.99
212	1342188055	2455178.11436	B	347.654	0.074	70.0	353.307	357.596	0.99
212	1342188055	2455178.11436	R	257.644	3.425	160.0	252.592	256.293	0.99
371	1342196724	2455336.47257	G	357.696	0.693	100.0	360.218	369.190	0.98
371	1342196724	2455336.47257	R	265.381	3.622	160.0	260.177	264.459	0.98
540	1342209039	2455505.54412	G	363.158	0.617	100.0	365.718	374.431	0.98
540	1342209039	2455505.54412	R	269.358	3.027	160.0	264.076	268.213	0.98
540	1342209042	2455505.55456	B	361.160	0.590	70.0	367.033	374.227	0.98
540	1342209042	2455505.55456	R	271.239	3.081	160.0	265.921	268.213	0.99
716	1342220894	2455681.48449	B	335.675	0.624	70.0	341.133	360.137	0.95
716	1342220894	2455681.48449	R	259.927	3.487	160.0	254.830	258.114	0.99
716	1342220897	2455681.49552	G	345.814	0.606	100.0	348.252	360.365	0.97
716	1342220897	2455681.49552	R	259.015	3.333	160.0	253.936	258.137	0.98
919	1342232522	2455884.64052	B	357.180	0.577	70.0	362.988	369.544	0.98
919	1342232522	2455884.64052	R	268.174	3.133	160.0	262.916	264.856	0.99
919	1342232525	2455884.65156	G	363.611	0.625	100.0	366.174	369.745	0.99
919	1342232525	2455884.65156	R	267.067	3.274	160.0	261.830	264.856	0.99
scan-map:									
173	1342186639	2455138.57697	B	366.234	0.953	70.0	372.189	373.735	1.00
173	1342186639	2455138.57697	R	272.688	0.578	160.0	267.341	267.860	1.00
173	1342186640	2455138.57977	B	365.895	0.996	70.0	371.844	373.735	0.99
173	1342186640	2455138.57977	R	274.044	0.409	160.0	268.671	267.860	1.00
173	1342186641	2455138.58258	G	369.927	0.892	100.0	372.535	373.938	1.00
173	1342186641	2455138.58258	R	270.638	0.587	160.0	265.331	267.860	0.99
173	1342186642	2455138.58538	G	370.323	0.500	100.0	372.934	373.938	1.00
173	1342186642	2455138.58538	R	272.891	0.516	160.0	267.540	267.860	1.00
212	1342188050	2455178.09582	G	353.854	0.820	100.0	356.348	357.790	1.00
212	1342188050	2455178.09582	R	261.431	0.542	160.0	256.305	256.293	1.00
212	1342188051	2455178.10019	G	353.944	0.852	100.0	356.439	357.790	1.00
212	1342188051	2455178.10019	R	261.651	0.578	160.0	256.521	256.293	1.00
212	1342188053	2455178.10727	B	346.981	0.796	70.0	352.623	357.596	0.99
212	1342188053	2455178.10727	R	261.247	0.643	160.0	256.125	256.293	1.00
212	1342188054	2455178.11165	B	347.727	0.816	70.0	353.381	357.596	0.99
212	1342188054	2455178.11165	R	261.144	0.583	160.0	256.024	256.293	1.00
371	1342196725	2455336.47648	G	363.033	0.828	100.0	365.592	369.190	0.99
371	1342196725	2455336.47648	R	267.308	0.569	160.0	262.067	264.459	0.99
371	1342196726	2455336.48041	G	362.101	0.844	100.0	364.654	369.190	0.99
371	1342196726	2455336.48041	R	268.028	0.649	160.0	262.773	264.459	0.99
371	1342196727	2455336.48433	B	356.769	0.784	70.0	362.570	368.989	0.98
371	1342196727	2455336.48433	R	268.451	0.667	160.0	263.187	264.459	1.00
371	1342196728	2455336.48825	B	356.584	0.805	70.0	362.382	368.989	0.98
371	1342196728	2455336.48825	R	268.881	0.658	160.0	263.609	264.459	1.00
540	1342209040	2455505.54803	G	369.456	0.834	100.0	372.060	374.431	0.99
540	1342209040	2455505.54803	R	270.919	0.671	160.0	265.607	268.213	0.99
540	1342209041	2455505.55196	G	368.218	0.483	100.0	370.814	374.431	0.99
540	1342209041	2455505.55196	R	270.729	0.588	160.0	265.421	268.213	0.99
540	1342209043	2455505.55848	B	362.158	0.786	70.0	368.047	374.227	0.98
540	1342209043	2455505.55848	R	272.120	0.671	160.0	266.784	268.213	0.99
540	1342209044	2455505.56241	B	362.000	0.656	70.0	367.886	374.227	0.98
540	1342209044	2455505.56241	R	271.890	0.602	160.0	266.559	268.213	0.99

continued on next page

Table 3. *continued*

OD	OBSID	observ. mid-time	PACS Band	Flux [Jy]	Unc. [Jy]	λ_{ref} [μm]	FD_{cc} [Jy]	FD_{model} [Jy]	Ratio $\text{FD}_{cc}/\text{FD}_{model}$
716	1342220895	2455681.48888	B	347.936	0.763	70.0	353.594	360.169	0.98
716	1342220895	2455681.48888	R	261.776	0.636	160.0	256.643	258.137	0.99
716	1342220896	2455681.49292	B	347.487	0.775	70.0	353.137	360.169	0.98
716	1342220896	2455681.49292	R	261.817	0.576	160.0	256.683	258.137	0.99
716	1342220898	2455681.49955	G	355.286	0.810	100.0	357.791	360.365	0.99
716	1342220898	2455681.49955	R	260.732	0.783	160.0	255.620	258.137	0.99
716	1342220899	2455681.50359	G	353.601	0.587	100.0	356.094	360.365	0.99
716	1342220899	2455681.50359	R	260.569	0.562	160.0	255.460	258.137	0.99
739	1342221604	2455705.06015	B	356.927	0.789	70.0	362.731	369.609	0.98
739	1342221604	2455705.06015	R	266.494	0.661	160.0	261.269	264.903	0.99
739	1342221605	2455705.06713	B	356.592	0.803	70.0	362.390	369.609	0.98
739	1342221605	2455705.06713	R	266.023	0.591	160.0	260.807	264.903	0.98
739	1342221606	2455705.07116	G	362.998	0.819	100.0	365.557	369.811	0.99
739	1342221606	2455705.07116	R	263.938	0.655	160.0	258.763	264.903	0.98
739	1342221607	2455705.07513	G	362.340	0.846	100.0	364.894	369.843	0.99
739	1342221607	2455705.07513	R	264.450	0.587	160.0	259.265	264.926	0.98
759	1342222561	2455724.68860	G	370.019	0.975	100.0	372.627	377.989	0.99
759	1342222561	2455724.68860	R	273.894	0.603	160.0	268.524	270.762	0.99
759	1342222562	2455724.72412	G	370.429	0.586	100.0	373.040	377.989	0.99
759	1342222562	2455724.72412	R	272.961	0.527	160.0	267.609	270.762	0.99
759	1342222563	2455724.75953	G	370.223	0.979	100.0	372.833	377.989	0.99
759	1342222563	2455724.75953	R	273.838	0.598	160.0	268.469	270.762	0.99
759	1342222564	2455724.79493	G	370.573	0.583	100.0	373.185	378.022	0.99
759	1342222564	2455724.79493	R	272.766	0.524	160.0	267.418	270.785	0.99
919	1342232523	2455884.64491	B	355.081	0.780	70.0	360.855	369.544	0.98
919	1342232523	2455884.64491	R	266.884	0.654	160.0	261.651	264.856	0.99
919	1342232524	2455884.64895	B	354.065	0.788	70.0	359.822	369.544	0.97
919	1342232524	2455884.64895	R	266.345	0.594	160.0	261.123	264.856	0.99
919	1342232526	2455884.65558	G	362.990	0.829	100.0	365.549	369.745	0.99
919	1342232526	2455884.65558	R	265.308	0.660	160.0	260.106	264.856	0.98
919	1342232527	2455884.65962	G	361.835	0.607	100.0	364.386	369.745	0.99
919	1342232527	2455884.65962	R	265.327	0.583	160.0	260.125	264.856	0.98
936	1342234207	2455901.05921	G	351.078	0.513	100.0	353.553	362.917	0.97
936	1342234207	2455901.05921	R	260.956	0.514	160.0	255.839	259.965	0.98
936	1342234208	2455901.09703	G	352.495	0.443	100.0	354.980	362.885	0.98
936	1342234208	2455901.09703	R	262.127	0.575	160.0	256.987	259.942	0.99
947	1342234435	2455912.34192	G	347.136	0.534	100.0	349.583	358.562	0.97
947	1342234435	2455912.34192	R	257.426	0.661	160.0	252.378	256.845	0.98
947	1342234436	2455912.37884	G	347.371	0.471	100.0	349.820	358.562	0.98
947	1342234436	2455912.37884	R	258.321	0.563	160.0	253.256	256.845	0.99
1119	1342246671	2456084.58171	G	368.955	0.842	100.0	371.556	375.056	0.99
1119	1342246671	2456084.58171	R	271.805	0.671	160.0	266.475	268.660	0.99
1119	1342246672	2456084.59417	G	367.594	0.487	100.0	370.185	375.056	0.99
1119	1342246672	2456084.59417	R	271.487	0.601	160.0	266.164	268.660	0.99
1119	1342246673	2456084.59822	B	359.597	0.793	70.0	365.444	374.852	0.97
1119	1342246673	2456084.59822	R	272.899	0.677	160.0	267.548	268.660	1.00
1119	1342246674	2456084.60226	B	359.418	0.737	70.0	365.262	374.852	0.97
1119	1342246674	2456084.60226	R	272.848	0.606	160.0	267.498	268.660	1.00
1287	1342255709	2456252.87637	G	362.095	0.828	100.0	364.648	369.713	0.99
1287	1342255709	2456252.87637	R	265.727	0.652	160.0	260.517	264.833	0.98
1287	1342255710	2456252.88317	G	360.922	0.597	100.0	363.466	369.713	0.98
1287	1342255710	2456252.88317	R	265.704	0.594	160.0	260.494	264.833	0.98
1287	1342255711	2456252.88729	B	352.586	0.780	70.0	358.319	369.511	0.97
1287	1342255711	2456252.88729	R	266.719	0.651	160.0	261.489	264.833	0.99
1287	1342255712	2456252.89133	B	352.057	0.719	70.0	357.781	369.479	0.97
1287	1342255712	2456252.89133	R	266.919	0.588	160.0	261.685	264.809	0.99
1444	1342270939	2456409.23071	G	350.582	0.667	100.0	353.053	358.112	0.99
1444	1342270939	2456409.23071	R	256.998	0.629	160.0	251.959	256.523	0.98
1444	1342270940	2456409.23766	G	349.436	0.580	100.0	351.899	358.112	0.98

continued on next page

Table 3. *continued*

OD	OBSID	observ. mid-time	PACS Band	Flux [Jy]	Unc. [Jy]	λ_{ref} [μm]	FD _{cc} [Jy]	FD _{model} [Jy]	Ratio FD _{cc} /FD _{model}
1444	1342270940	2456409.23766	R	259.081	0.582	160.0	254.001	256.523	0.99
1444	1342270941	2456409.24170	B	341.380	0.681	70.0	346.931	357.917	0.97
1444	1342270941	2456409.24170	R	258.577	0.626	160.0	253.507	256.523	0.99
1444	1342270942	2456409.24574	B	340.622	0.623	70.0	346.161	357.917	0.97
1444	1342270942	2456409.24574	R	260.128	0.578	160.0	255.027	256.523	0.99

Appendix A: Bright-source measurements

In the following tables we list the available photometric observations of the bright sources, mainly related to calibration programs. Only Uranus and Neptune were observed in the PACS photometer chop-nod observing mode (point-source mode) with dithering (Table A.1). Both sources were measured in all three bands, some in low, some in high gain, each time only in a single repetition of the pre-defined dithered chop-nod pattern.

On-source scan-map observations were taken for Mars, Uranus, Neptune, Callisto, Ganymede, and Titan (Table A.2). These measurements cover different instrument settings (bands, gain, scan-speed, map settings), and different fields on sky. The source is usually close to the map center (solar system object tracking mode), only one set of Neptune measurements was taken in fixed mode with the source located off-center, but still well within the final maps. The Callisto and Ganymede observations were also taken in fixed mode, but with both sources close to the map center. The Mars measurements are heavily saturated, and it is not possible to extract meaningful fluxes.

In the HSA one set of measurements is labeled "Saturn scan" and another "Uranus 2012-01-07" and "Uranus 2012-01-13". They were taken in fixed mode and as part of a science project (Table A.3). In these measurements only off-source fields were scanned and only parts of the PSF wings are visible in one corner of the maps (Figure A.1). The data are part of a science program aiming at the detection of dust rings from irregular satellites.

Table A.1. Herschel-PACS photometer **chop-nod** observations (proposals Calibration_pypacs_## and Calibration_rppacs_###), taken in point-source observing mode with dithering and solar system object (SSO) tracking mode. SAA: solar aspect angle; dur.: duration of observation in seconds; fil.: filter/band combination (B: 70/160 μm ; G: 100/160 μm); G.: low (L) or high (H) gain; R: repetition of entire chop-nod pattern; r: heliocentric distance; Δ : Herschel-centric distance; α : phase angle; diam.: effective angular diameter⁽¹⁾.

OD	OBSID	Target	SAA [$^{\circ}$]	UTC Start time yyyy mon dd hh:mm:ss	dur. [s]	fil.	G.	R.	r [AU]	Δ [AU]	α [$^{\circ}$]	diam. ⁽¹⁾ [$''$]
212	1342188056	Uranus	-1.9	2009 Dec 12 14:52:22	171	B/R	L	1	20.09716	20.04905	3.00	3.476
212	1342188057	Uranus	-1.9	2009 Dec 12 14:56:16	171	G/R	L	1	20.09716	20.04909	3.00	3.476
579	1342211116	Uranus	-5.6	2010 Dec 13 17:09:40	162	B/R	L	1	20.08994	19.97489	2.83	3.487
579	1342211119	Uranus	-5.0	2010 Dec 13 17:26:36	162	G/R	L	1	20.08994	19.97509	2.83	3.487
789	1342223981	Uranus	-14.3	2011 Jul 12 01:15:35	162	B/R	L	1	20.08320	19.80140	2.84	3.524
789	1342223984	Uranus	-14.4	2011 Jul 12 01:32:07	162	G/R	L	1	20.08320	19.80121	2.84	3.524
957	1342235628	Uranus	-5.1	2011 Dec 26 22:27:18	162	B/R	L	1	20.07648	20.11786	2.83	3.464
957	1342235631	Uranus	4.0	2011 Dec 26 22:55:25	162	G/R	L	1	20.07648	20.11820	2.83	3.464
173	1342186637	Neptune	-10.5	2009 Nov 03 01:35:52	171	B/R	H	1	30.02612	29.79070	1.86	2.277
173	1342186638	Neptune	-12.5	2009 Nov 03 01:45:23	171	G/R	H	1	30.02611	29.79081	1.86	2.277
173	1342186643	Neptune	-12.5	2009 Nov 03 02:05:25	171	G/R	L	1	30.02611	29.79104	1.86	2.277
212	1342188052	Neptune	26.7	2009 Dec 12 14:26:45	171	G/R	H	1	30.02504	30.45664	1.70	2.227
212	1342188055	Neptune	26.7	2009 Dec 12 14:43:15	171	B/R	H	1	30.02504	30.45682	1.70	2.227
371	1342196724	Neptune	-0.1	2010 May 19 23:19:09	162	G/R	H	1	30.02059	29.99826	1.95	2.262
540	1342209039	Neptune	-13.0	2010 Nov 05 01:02:11	162	G/R	H	1	30.01563	29.77119	1.86	2.278
540	1342209042	Neptune	-13.0	2010 Nov 05 01:17:13	162	B/R	L	1	30.01563	29.77137	1.86	2.278
716	1342220894	Neptune	21.3	2011 Apr 29 23:36:19	162	B/R	L	1	30.01024	30.36190	1.81	2.235
716	1342220897	Neptune	21.3	2011 Apr 29 23:52:12	162	G/R	H	1	30.01024	30.36173	1.81	2.235
919	1342232522	Neptune	-1.5	2011 Nov 19 03:21:00	162	B/R	L	1	30.00382	29.95799	1.91	2.264
919	1342232525	Neptune	-1.5	2011 Nov 19 03:36:54	162	G/R	H	1	30.00381	29.95818	1.91	2.264

Notes. ⁽¹⁾ Taken from "diam.dat", provided by R. Moreno, Jul. 25, 2012 to the Herschel Calibration Steering Group Team, taking into account the equatorial and polar radii and the sub-observer latitude.

Table A.2. Herschel-PACS photometer **scan-map** observations (proposal Calibration_pvpacs_###, Calibration_rppacs_###, OT1_ddan01_1), taken in large-scan observing mode, SSO tracking (exceptions see footnote), i.e., with the target located well within the observed field. SAA: solar aspect angle; dur.: duration of observation in seconds; fil.: filter/band combination (B: 70/160 μm ; G: 100/160 μm); G.: low (L) or high (H) gain; R.: repetition of entire scan map; S.: scan-speed in $''/\text{s}$, scan-map parameters; Len: scan-leg length (in arc min) \times n: number of scan legs \times sep: scan-leg separation (in arc sec); ang.: satellite scan angle in degrees with respect to instrument reference frame; r: heliocentric distance; Δ : heliocentric distance; α : phase angle; diam: effective angular diameter¹.

OD	OBSID	Target	SAA [$^\circ$]	UTC Start time yyyy mon dd	hh:mm:ss	dur. [s]	fil.	G.	R.	S. [$''/\text{s}$]	Len \times n \times sep [$'\times\#\times''$]	ang. [$^\circ$]	r [AU]	Δ [AU]	α [$^\circ$]	diam ¹ [$''$]
888	1342231157 ²	Mars	22.8	2011 Oct 19	06:44:59	3729	B/R	H	1	60	80 \times 21 \times 20	45	1.59877	1.68205	35.60	5.568
888	1342231158 ²	Mars	22.1	2011 Oct 19	07:49:26	3729	B/R	H	1	60	80 \times 21 \times 20	135	1.59882	1.68171	35.61	5.569
888	1342231159 ²	Mars	22.1	2011 Oct 19	08:52:45	3729	B/R	H	1	60	80 \times 21 \times 20	225	1.59886	1.68138	35.61	5.570
888	1342231160 ²	Mars	22.8	2011 Oct 19	09:56:04	3729	B/R	H	1	60	80 \times 21 \times 20	315	1.59891	1.68104	35.61	5.571
888	1342231161 ²	Mars	22.8	2011 Oct 19	10:59:23	3729	G/R	H	1	60	80 \times 21 \times 20	45	1.59895	1.68071	35.62	5.572
888	1342231162 ²	Mars	22.0	2011 Oct 19	12:02:42	3729	G/R	H	1	60	80 \times 21 \times 20	135	1.59900	1.68037	35.62	5.573
888	1342231163 ²	Mars	22.1	2011 Oct 19	13:06:01	3729	G/R	H	1	60	80 \times 21 \times 20	225	1.59905	1.68004	35.63	5.574
888	1342231164 ²	Mars	22.7	2011 Oct 19	14:09:21	3729	G/R	H	1	60	80 \times 21 \times 20	315	1.59909	1.67971	35.63	5.576
906	1342231949 ²	Mars	14.5	2011 Nov 06	04:07:04	3245	B/R	H	1	20	20 \times 41 \times 6	90	1.61655	1.53977	36.93	6.082
906	1342231950 ²	Mars	14.5	2011 Nov 06	05:05:20	3245	G/R	H	1	20	20 \times 41 \times 6	90	1.61658	1.53944	36.93	6.084
579	1342211117	Uranus	-5.2	2010 Dec 13	17:15:17	286	B/R	L	1	20	3.0 \times 10 \times 4	70	20.08994	19.97497	2.83	3.487
579	1342211118	Uranus	-5.2	2010 Dec 13	17:21:06	286	B/R	L	1	20	3.0 \times 10 \times 4	110	20.08994	19.97504	2.83	3.487
579	1342211120	Uranus	-5.2	2010 Dec 13	17:30:40	286	G/R	L	1	20	3.0 \times 10 \times 4	70	20.08994	19.97515	2.83	3.487
579	1342211121	Uranus	-5.2	2010 Dec 13	17:36:29	286	G/R	L	1	20	3.0 \times 10 \times 4	110	20.08994	19.97522	2.83	3.487
789	1342223982	Uranus	-14.5	2011 Jul 12	01:21:03	286	B/R	L	1	20	3.0 \times 10 \times 4	70	20.08320	19.80132	2.84	3.524
789	1342223983	Uranus	-14.5	2011 Jul 12	01:26:52	286	B/R	L	1	20	3.0 \times 10 \times 4	110	20.08320	19.80126	2.84	3.524
789	1342223985	Uranus	-14.5	2011 Jul 12	01:36:26	286	G/R	L	1	20	3.0 \times 10 \times 4	70	20.08320	19.80115	2.84	3.524
789	1342223986	Uranus	-14.5	2011 Jul 12	01:42:15	286	G/R	L	1	20	3.0 \times 10 \times 4	110	20.08320	19.80108	2.84	3.524
957	1342235629	Uranus	3.8	2011 Dec 26	22:44:31	286	B/R	L	1	20	3.0 \times 10 \times 4	70	20.07648	20.11808	2.83	3.464
957	1342235630	Uranus	3.8	2011 Dec 26	22:50:20	286	B/R	L	1	20	3.0 \times 10 \times 4	110	20.07648	20.11815	2.83	3.464
957	1342235632	Uranus	3.8	2011 Dec 26	22:59:54	286	G/R	L	1	20	3.0 \times 10 \times 4	70	20.07648	20.11826	2.83	3.464
957	1342235633	Uranus	3.8	2011 Dec 26	23:05:43	286	G/R	L	1	20	3.0 \times 10 \times 4	110	20.07648	20.11833	2.83	3.464
1121	1342246772	Uranus	20.5	2012 Jun 08	04:24:01	286	B/R	L	1	20	3.0 \times 10 \times 4	70	20.06880	20.40446	2.74	3.421
1121	1342246773	Uranus	20.5	2012 Jun 08	04:29:50	286	B/R	L	1	20	3.0 \times 10 \times 4	110	20.06880	20.40439	2.74	3.421
1121	1342246774	Uranus	20.5	2012 Jun 08	04:35:39	286	G/R	L	1	20	3.0 \times 10 \times 4	70	20.06880	20.40433	2.74	3.421
1121	1342246775	Uranus	20.5	2012 Jun 08	04:41:28	286	G/R	L	1	20	3.0 \times 10 \times 4	110	20.06880	20.40427	2.74	3.421
1310	1342257193	Uranus	-12.3	2012 Dec 14	01:43:37	286	B/R	L	1	20	3.0 \times 10 \times 4	70	20.05868	19.82251	2.77	3.517
1310	1342257194	Uranus	-12.3	2012 Dec 14	01:49:26	286	B/R	L	1	20	3.0 \times 10 \times 4	110	20.05868	19.82258	2.77	3.517
1310	1342257195	Uranus	-12.3	2012 Dec 14	01:55:15	286	G/R	L	1	20	3.0 \times 10 \times 4	70	20.05868	19.82265	2.77	3.517
1310	1342257196	Uranus	-12.3	2012 Dec 14	02:01:04	286	G/R	L	1	20	3.0 \times 10 \times 4	110	20.05868	19.82272	2.77	3.517
173	1342186639	Neptune	-12.5	2009 Nov 03	01:49:21	179	B/R	L	1	20	5.0 \times 4 \times 51	45	30.02611	29.79086	1.86	2.277
173	1342186640	Neptune	-12.5	2009 Nov 03	01:53:23	179	B/R	L	1	20	5.0 \times 4 \times 51	135	30.02611	29.79090	1.86	2.277
173	1342186641	Neptune	-12.4	2009 Nov 03	01:57:25	179	G/R	H	1	20	5.0 \times 4 \times 51	45	30.02611	29.79095	1.86	2.277
173	1342186642	Neptune	-12.5	2009 Nov 03	02:01:27	179	G/R	H	1	20	5.0 \times 4 \times 51	135	30.02611	29.79100	1.86	2.277
212	1342188050	Neptune	26.7	2009 Dec 12	14:15:21	315	G/R	H	1	20	4.0 \times 8 \times 4	63	30.02504	30.45653	1.70	2.227
212	1342188051	Neptune	26.7	2009 Dec 12	14:21:39	315	G/R	H	1	20	4.0 \times 8 \times 4	117	30.02504	30.45660	1.70	2.227
212	1342188053	Neptune	26.7	2009 Dec 12	14:31:51	315	B/R	H	1	20	4.0 \times 8 \times 4	63	30.02504	30.45671	1.70	2.227

continued on next page

Table A.2. *continued*

OD	OBSID	Target	SAA [°]	UTC Start time yyyy mon dd hh:mm:ss	dur. [s]	fil.	G.	R.	S. ["/s]	LenXnXsep [' × # × '']	ang. [°]	r [AU]	Δ [AU]	α [°]	diam/ ["']
212	1342188054	Neptune	26.7	2009 Dec 12 14:38:09	315	B/R	H	1	20	4.0 × 8 × 4	117	30.02504	30.45678	1.70	2.227
371	1342196725	Neptune	-0.1	2010 May 19 23:23:50	276	G/R	H	1	20	2.5 × 10 × 4	70	30.02059	29.99819	1.95	2.262
371	1342196726	Neptune	-0.1	2010 May 19 23:29:29	276	G/R	H	1	20	2.5 × 10 × 4	110	30.02059	29.99813	1.95	2.262
371	1342196727	Neptune	-0.1	2010 May 19 23:35:08	276	B/R	L	1	20	2.5 × 10 × 4	70	30.02059	29.99806	1.95	2.262
371	1342196728	Neptune	-0.1	2010 May 19 23:40:47	276	B/R	L	1	20	2.5 × 10 × 4	110	30.02059	29.99799	1.95	2.262
540	1342209040	Neptune	-13.0	2010 Nov 05 01:06:52	276	G/R	H	1	20	2.5 × 10 × 4	70	30.01563	29.77126	1.86	2.278
540	1342209041	Neptune	-13.0	2010 Nov 05 01:12:31	276	G/R	H	1	20	2.5 × 10 × 4	110	30.01563	29.77133	1.86	2.278
540	1342209043	Neptune	-13.0	2010 Nov 05 01:21:55	276	B/R	L	1	20	2.5 × 10 × 4	70	30.01563	29.77144	1.86	2.278
540	1342209044	Neptune	-13.0	2010 Nov 05 01:27:34	276	B/R	L	1	20	2.5 × 10 × 4	110	30.01563	29.77150	1.86	2.278
716	1342220895	Neptune	21.3	2011 Apr 29 23:41:36	286	B/R	L	1	20	3.0 × 10 × 4	70	30.01024	30.36183	1.81	2.235
716	1342220896	Neptune	21.3	2011 Apr 29 23:47:25	286	B/R	L	1	20	3.0 × 10 × 4	110	30.01024	30.36177	1.81	2.235
716	1342220898	Neptune	21.3	2011 Apr 29 23:56:58	286	G/R	H	1	20	3.0 × 10 × 4	70	30.01024	30.36167	1.81	2.235
716	1342220899	Neptune	21.3	2011 Apr 30 00:02:47	286	G/R	H	1	20	3.0 × 10 × 4	110	30.01024	30.36160	1.81	2.235
739	1342221604	Neptune	-0.0	2011 May 23 13:24:14	286	B/R	L	1	20	3.0 × 10 × 4	70	30.00950	29.97101	1.96	2.264
739	1342221605	Neptune	-1.0	2011 May 23 13:34:17	286	B/R	L	1	20	3.0 × 10 × 4	110	30.00950	29.97089	1.96	2.264
739	1342221606	Neptune	-1.0	2011 May 23 13:40:05	286	G/R	H	1	20	3.0 × 10 × 4	70	30.00950	29.97082	1.96	2.264
739	1342221607	Neptune	-1.0	2011 May 23 13:45:48	286	G/R	H	1	20	3.0 × 10 × 4	110	30.00950	29.97075	1.96	2.264
759	1342222561	Neptune	-19.6	2011 Jun 12 04:06:37	2996	G/R	H	4	20	7.0 × 18 × 25	45	30.00889	29.64553	1.85	2.289
759	1342222562	Neptune	-19.7	2011 Jun 12 04:57:46	2996	G/R	H	4	20	7.0 × 18 × 25	135	30.00889	29.64497	1.85	2.289
759	1342222563	Neptune	-19.7	2011 Jun 12 05:48:45	2996	G/R	H	4	20	7.0 × 18 × 25	45	30.00889	29.64440	1.85	2.289
759	1342222564	Neptune	-19.8	2011 Jun 12 06:39:44	2996	G/R	H	4	20	7.0 × 18 × 25	135	30.00888	29.64384	1.85	2.289
919	1342232523	Neptune	-1.5	2011 Nov 19 03:26:17	286	B/R	L	1	20	3.0 × 10 × 4	70	30.00381	29.95807	1.91	2.264
919	1342232524	Neptune	-1.5	2011 Nov 19 03:32:06	286	B/R	L	1	20	3.0 × 10 × 4	110	30.00381	29.95814	1.91	2.264
919	1342232526	Neptune	-1.5	2011 Nov 19 03:41:39	286	G/R	H	1	20	3.0 × 10 × 4	70	30.00381	29.95825	1.91	2.264
919	1342232527	Neptune	-1.5	2011 Nov 19 03:47:28	286	G/R	H	1	20	3.0 × 10 × 4	110	30.00381	29.95832	1.91	2.264
936	1342234207 ³	Neptune	14.8	2011 Dec 05 13:00:23	2986	G/R	H	4	20	7.0 × 18 × 25	45	30.00329	30.23924	1.84	2.243
936	1342234208 ³	Neptune	14.9	2011 Dec 05 13:54:50	2986	G/R	H	4	20	7.0 × 18 × 25	135	30.00329	30.23988	1.84	2.243
947	1342234435 ³	Neptune	26.0	2011 Dec 16 19:47:29	2986	G/R	H	4	20	7.0 × 18 × 25	45	30.00293	30.42232	1.71	2.229
947	1342234436 ³	Neptune	26.0	2011 Dec 16 20:40:39	2986	G/R	H	4	20	7.0 × 18 × 25	135	30.00293	30.42290	1.71	2.229
1097	1342245787 ⁴	Neptune	8.2	2012 May 15 07:25:59	286	G/R	H	1	20	3.0 × 10 × 4	70	29.99809	30.12620	1.93	2.252
1097	1342245788 ⁴	Neptune	8.1	2012 May 15 07:31:48	286	G/R	H	1	20	3.0 × 10 × 4	110	29.99809	30.12614	1.93	2.252
1097	1342245789 ⁴	Neptune	8.1	2012 May 15 07:37:37	286	B/R	L	1	20	3.0 × 10 × 4	70	29.99809	30.12607	1.93	2.252
1097	1342245790 ⁴	Neptune	8.1	2012 May 15 07:43:26	286	B/R	L	1	20	3.0 × 10 × 4	110	29.99808	30.12600	1.93	2.252
1119	1342246671	Neptune	-12.3	2012 Jun 06 01:55:17	286	G/R	H	1	20	3.0 × 10 × 4	70	29.99739	29.75976	1.92	2.280
1119	1342246672	Neptune	-12.3	2012 Jun 06 02:13:13	286	G/R	H	1	20	3.0 × 10 × 4	110	29.99738	29.75956	1.92	2.280
1119	1342246673	Neptune	-12.3	2012 Jun 06 02:19:03	286	B/R	L	1	20	3.0 × 10 × 4	70	29.99738	29.75949	1.92	2.280
1119	1342246674	Neptune	-12.3	2012 Jun 06 02:24:52	286	B/R	L	1	20	3.0 × 10 × 4	110	29.99738	29.75943	1.92	2.280
1287	1342255709	Neptune	1.6	2012 Nov 21 08:59:35	286	G/R	H	1	20	3.0 × 10 × 4	70	29.99197	29.95865	1.91	2.264
1287	1342255710	Neptune	-0.8	2012 Nov 21 09:09:23	286	G/R	H	1	20	3.0 × 10 × 4	110	29.99197	29.95877	1.91	2.264
1287	1342255711	Neptune	-0.8	2012 Nov 21 09:15:19	286	B/R	L	1	20	3.0 × 10 × 4	70	29.99197	29.95884	1.91	2.264
1287	1342255712	Neptune	-0.8	2012 Nov 21 09:21:08	286	B/R	L	1	20	3.0 × 10 × 4	110	29.99197	29.95891	1.91	2.264
1444	1342270939	Neptune	24.6	2013 Apr 26 17:29:50	286	G/R	H	1	20	3.0 × 10 × 4	70	29.98701	30.45382	1.71	2.228

continued on next page

Table A.2. *continued*

OD	OBSID	Target	SAA [°]	UTC Start time yy yy mon dd hh:mm:ss	dur. [s]	fil.	G.	R.	S. ["/s]	Len×n×sep [' × # × "']	ang. [°]	r [AU]	Δ [AU]	α [°]	diam/ ["']
1444	1342270940	Neptune	28.3	2013 Apr 26 17:39:51	286	G/R	H	1	20	3.0 × 10 × 4	110	29.98701	30.45372	1.71	2.228
1444	1342270941	Neptune	28.3	2013 Apr 26 17:45:40	286	B/R	L	1	20	3.0 × 10 × 4	70	29.98701	30.45365	1.71	2.228
1444	1342270942	Neptune	28.3	2013 Apr 26 17:51:29	286	B/R	L	1	20	3.0 × 10 × 4	110	29.98701	30.45359	1.71	2.228
981	1342238042 ⁵	Callisto	-2.0	2012 Jan 20 05:29:58	3114	B/R	L	1	10	2.0 × 120 × 2	0	4.98332	4.85010	11.47	1.370
981	1342238043 ⁵	Callisto	-1.9	2012 Jan 20 06:22:55	2274	B/R	L	1	10	4.0 × 60 × 2	90	4.98345	4.85072	11.47	1.370
981	1342238042 ⁶	Ganymede	-2.0	2012 Jan 20 05:29:58	3114	B/R	L	1	10	2.0 × 120 × 2	0	4.97487	4.84122	11.50	1.499
981	1342238043 ⁶	Ganymede	-1.9	2012 Jan 20 06:22:55	2274	B/R	L	1	10	4.0 × 60 × 2	90	4.97508	4.84194	11.50	1.499
1138	1342247418	Titan	-18.3	2012 Jun 25 15:22:31	286	B/R	H	1	20	3.0 × 10 × 4	70	9.74085	9.36711	5.73	0.758
1138	1342247419	Titan	-18.3	2012 Jun 25 15:28:20	286	B/R	H	1	20	3.0 × 10 × 4	110	9.74087	9.36719	5.73	0.758
1138	1342247420	Titan	-18.3	2012 Jun 25 15:34:09	286	G/R	H	1	20	3.0 × 10 × 4	70	9.74088	9.36726	5.73	0.758
1138	1342247421	Titan	-18.3	2012 Jun 25 15:39:58	286	G/R	H	1	20	3.0 × 10 × 4	110	9.74089	9.36733	5.73	0.758

Notes.

(¹) for Uranus and Neptune taken from "diam.dat", provided by R. Moreno, Jul. 25, 2012; otherwise from JPL Horizons.

(²) central part of the source is clearly saturated.

(³) observations are made in fixed mode without tracking, Neptune is located fully inside the field of view, but toward one corner of the map.

(⁴) data are labeled "FAILED" in the HSA.

(⁵) observations are made in fixed mode without tracking, Callisto is located off center.

(⁶) observations are made in fixed mode without tracking, Ganymede is located off center.

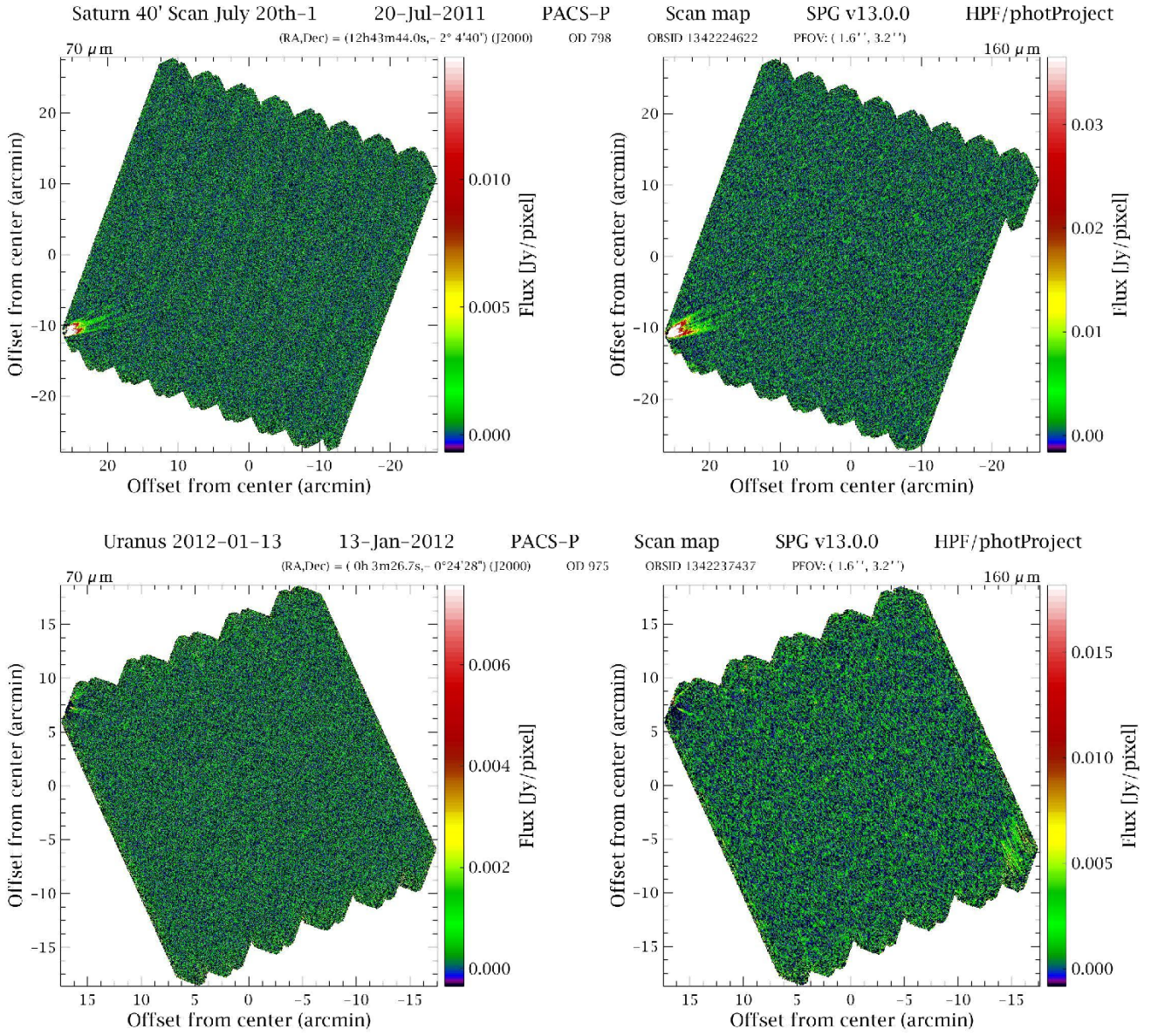


Fig. A.1. Top: HSA maps of OBSID 1342224622 with Saturn located outside the field of view in the lower left corner. Bottom: HSA maps of OBSID 1342237437 with Uranus located outside the field of view beyond the upper left corner. These measurements are only useful for off-source investigations in the planet's direct vicinity.

Table A.3. Additional Herschel-PACS photometer scan-map observations related to the bright planets and planetary satellites (proposals OT1_ddan01_1), taken in large-scan observing mode without SSO tracking (fixed mode), and high gain. The planets were located at the edge or outside the observed field of view. SAA: solar aspect angle; dur.: duration of observation in seconds; fil.: filter/band combination (B: 70/160 μm ; G: 100/160 μm); G.: low (L) or high (H) gain; R.: repetition of entire scan map; S.: satellite scan speed: 20"/s or 60"/s; scan-map parameters: Len: scan-leg length (in arc min) \times n: number of scan legs \times sep: scan-leg separation (in arc sec); ang.: satellite scan angle in degrees with respect to instrument reference frame; r: heliocentric distance; Δ : Herschel-centric distance; α : phase angle; diam: effective angular diameter.

OD	OBSID	Target	SAA [$^{\circ}$]	UTC Start time	dur. [s]	fil.	G.	R.	S. ["/s]	Len \times n \times sep [' \times # \times "']	ang. [$^{\circ}$]	r [AU]	Δ [AU]	α [$^{\circ}$]	diam ["']
798	1342224620	Saturn	16.5	2011 Jul 20 19:02:46	1732	B/R	H	4	20	15 \times 1 \times 2	45	9.64468	9.87529	5.87	16.829
798	1342224621	Saturn	16.5	2011 Jul 20 19:33:38	1732	B/R	H	4	20	15 \times 1 \times 2	135	9.64469	9.87569	5.86	16.829
798	1342224622	Saturn	16.5	2011 Jul 20 20:08:29	2325	B/R	H	1	20	40 \times 1 \times 2	45	9.64469	9.87611	5.86	16.828
798	1342224623	Saturn	16.9	2011 Jul 20 20:48:17	2325	B/R	H	1	20	40 \times 1 \times 2	135	9.64470	9.87656	5.86	16.827
807	1342224837	Saturn	24.3	2011 Jul 29 13:14:30	1732	B/R	H	4	20	15 \times 1 \times 2	45	9.64724	10.01382	5.58	16.597
807	1342224838	Saturn	24.3	2011 Jul 29 13:45:40	1732	B/R	H	4	20	15 \times 1 \times 2	135	9.64725	10.01414	5.57	16.596
807	1342224839	Saturn	24.3	2011 Jul 29 14:20:31	2325	B/R	H	1	20	40 \times 1 \times 2	45	9.64726	10.01457	5.57	16.595
807	1342224840	Saturn	24.7	2011 Jul 29 15:00:19	2325	B/R	H	1	20	40 \times 1 \times 2	135	9.64726	10.01500	5.57	16.595
969	1342236891	Uranus	15.7	2012 Jan 07 11:26:54	3061	B/R	H	3	20	25 \times 1 \times 2	45	20.07598	20.31566	2.73	3.469
969	1342236892	Uranus	15.8	2012 Jan 07 12:20:10	3061	B/R	H	3	20	25 \times 1 \times 2	135	20.07598	20.31629	2.73	3.469
975	1342237436	Uranus	21.8	2012 Jan 13 11:59:55	3061	B/R	H	3	20	25 \times 1 \times 2	45	20.07571	20.41527	2.64	3.452
975	1342237437	Uranus	21.7	2012 Jan 13 12:52:30	3061	B/R	H	3	20	25 \times 1 \times 2	135	20.07571	20.41587	2.64	3.452